 doi:10.20944/preprints202011.0740.v1

Article

Detonation Nanodiamonds: A Comparison Study by Photoacoustic, Diffuse Reflectance, and Attenuated Total Reflection FTIR spectroscopies

Dmitry S. Volkov *, Petr K. Krivoshein, and Mikhail A. Proskurnin *

Chemistry Department, Lomonosov Moscow State University, Moscow, 119991, Russia
* Correspondence: dmsvolkov@gmail.com; proskurnin@gmail.com.

Abstract: The qualitative analysis of nanodiamonds by FTIR spectrometry as photoacoustic (PAS), diffuse-reflectance (DRIFT), and attenuated total reflection (ATR) modalities was evaluated for rapid and nondestructive analysis and comparison of nanodiamonds. The spectra reproducibility and signal-gathering depth was compared. The assignment of characteristic bands showed that only six groups of bands were present in spectra of all the modalities with appropriate sensitivity: 1760 (C=O stretch, isolated carboxyl groups); 1640–1632 (H–O–H bend, liquid water); 1400–1370 (non-carboxyl C–O–H in-plane bend and CH_2 deformation); 1103 (non-carboxyl C–O stretch); 1060 (in-plane C–H bend, non-aromatic hydrocarbons and carbohydrates); and 940 cm^{-1} (out-of-plane carboxyl C–O–H bend). DRIFT provides the maximum number of bands and is capable of measuring hydrogen-bonded bands and CHX groups. ATR provides the good sensitivity for water and C–H/C–C bands in the range 2000–400 cm^{-1}. PAS-FTIR reveals less bands than DRIFT but more intense bands than ATR-FTIR and shows the maximum sensitivity for absorption bands that do not appear in ATR-IR spectra and are expedient for supporting either DRIFT or PAS along with depth-profiling. Thus, all three modalities are required for full characterization of nanodiamonds surface functional groups.

Keywords: detonation nanodiamonds, photoacoustic IR spectroscopy; diffuse-reflectance IR spectroscopy, attenuated total internal reflection IR spectroscopy

1. Introduction

Nanodiamonds (ND), due to the nanometer size of their primary particles, have a surface with a significant area and a large number of functional groups [1, 2]. During the production cycle, the initial charge goes through several stages of chemical treatment, mainly of an oxidizing nature. This is necessary primarily for the removal of non-diamond forms of carbon. As a result, various functional groups form at the surface of nanodiamonds, which are responsible for the use of nanodiamonds as sorbents [1, 3-5] and crucial for technological and biomedical applications of nanodiamonds [6-11].

FTIR spectroscopy, usually in the mid-IR region, is widely used to characterize nanodiamonds and their surface groups [12]. Previous articles on the surface groups of nanodiamonds by FTIR are mostly based on sample-pellet transmission FTIR techniques [4]; less common are diffuse reflectance FTIR (DRIFT) [13] or attenuated total reflectance FTIR (ATR-FTIR) [14, 15]. However, there are a number of contradictions in the selection and assignment of the main absorption bands of nanodiamonds, a unified scheme of sample preparation for the analysis of nanodiamonds has not been proposed, and no rather wide comparative data on different samples or brands of nanodiamonds exist.

Transmission FTIR methods with pellets work with several milligrams of nanodiamond sample and *ca.* 150 mg of KBr or KCl, which are selected for the implementation of the Bouguer-Lambert-Beer law. The distribution of KBr particles and the test object should be uniform for better comparison between measurements [16]. Another disadvantage is the high hygroscopicity

Preprints (www.preprints.org) | NOT PEER-REVIEWED | Posted: 30 November 2020 doi:10.20944/preprints202011.0740.v1

of KBr and KCl and the possible reactions of alkali metal halides with surface groups of nanodiamonds, the probability of which increases with grinding-assisted mechanochemistry of nanodiamonds with alkali metal halides [14]. KBr also absorbs radiation in the far infrared region, which does not allow measurements below 400 cm^{-1} [17]; KBr or KCl should also be of an acceptable purity.

DRIFT is not the most common method for studying the surface of nanodiamonds due to the sensitivity to the particle distribution in the sample holder, the width of the nanodiamonds fraction; these features lead to low reproducibility of this method [13, 18]. As transmission techniques, DRIFT requires the dilution of the test nanodiamond sample with KBr or KCl and subsequent grinding.

ATR-FTIR spectrometry is considered the most convenient selection for ND surfaces due to its simplicity and as it provides spectra comparable with the transmission spectra [7, 19, 20]. It does not require the sample dilution, which opens the far IR region. This method also allows varying the depth of radiation penetration into the sample by changing the incidence angle of the radiation, but this feature is not implemented in most ATR units [21]. Also, it is considered that ND films and powders have the optimum particle size to achieve a good covering of the ATR crystal surface and sufficient adhesion. However, ATR-FTIR has several limitations. This method requires full contact of the test sample with the ATR crystal to improve the signal-to-noise ratio [16]. As diamond is one of the hardest materials, the good contact between the NDs and the ATR crystal is a problem: such materials as ZnSe, Ge, or KRS-5 are too soft and their surface at a considerable pressure of the ATR press can be damaged. In addition, a part of the ND sample may retain in the crystal, leading to fast degradation of the crystal operability. Thus, for NDs, only a diamond ATR crystal is applicable, but it does not allow measuring the diamond itself, thus, the absorption of surface ND groups may be acquired. The recording of the ATR-IR spectra of nanodiamonds without using a clamping screw are described [22]: a colloidal solution of nanodiamonds is prepared in a highly volatile solvent placed to the crystal, after drying, ATR-FTIR spectra are recorded. In addition, raw ATR-FTIR spectra are usually strongly distorted: shifts to lower wavenumbers are observed. This requires extra (extended) ATR correction [16], but the parameters for this mathematical transform are selected manually, often empirically; therefore, some information may be degraded or warped.

Interferometer-based FTIR photoacoustic spectroscopy (PAS-FTIR) is a developed instrument for complex samples [23-27]. It can be used for mineral, polymer, and technological samples. Some capabilities of PAS-FTIR are analogous to ATR-IR and some, to DRIFT. As ATR-FTIR, it does not need sample dilution and is applicable in the far IR region. PAS-FTIR has some advantages. It allows varying the depth of radiation penetration by changing the modulation frequency, which provides a longer range of depths. PAS-FTIR was used to crushed diamonds down to a micron size [28], PAS-FTIR and DRIFT methods showed comparable results [29]. However, as far as we know, PAS-FTIR method was not used to date for studying the surface of nanodiamonds. The whole comparison of various modalities for complex samples (biochars, soils) has recently become a topic of several review or feature papers [30, 31], however, usually the research is focused on specific characteristic like depth profiling in PAS [27, 32, 33]. For nanodiamonds, as far as we are concerned, a full comparison of PAS, DRIFT and ATR features in spectral information was not done.

The growing number of studies dealing with various modifications of the nanodiamond surface makes serious demands on the methods of surface characterization. Thus, the aim of this work was to compare the spectral information provided by these modalities for the same samples measured under the same conditions. To assess their capabilities from the point of view of maximum information content and reliability of the spectral information provided, we studied the surface of NDs using ATR-FTIR, DRIFT, and PAS-FTIR and compared the results for a rather wide selection of various ND brands.

2. Materials and Methods

2.1 Nanodiamonds

Preprints (www.preprints.org) | NOT PEER-REVIEWED | Posted: 30 November 2020 doi:10.20944/preprints202011.0740.v1

We used commercially available NDs, summed up in Table 1. Powders from aqueous suspension (SDND, PL-Nanopure-G01P) stock solutions were prepared by drying in a drying oven (SNOL 20/300, Snol-Therm) at 100°C. For analysis nanodiamonds powder were used as is or were gently ground in a jasper mortar.

Table 1. Nanodiamonds used in the survey

Product name	Description	Manufacturer
RDDM	detonation polycrystalline diamond of RDDM grade, fraction 0–0.125	«Real-Dzerzhinsk» Ltd., Dzerzhinsk, Russia
RUDDM a	nanodiamond material of RUDDM grade, fraction 0–150	
SDND	5 wt. % Single-Digit NanoDiamonds aqueous suspension	PlasmaChem GmbH, Germany
PL-D-G	Purified powder grade G	
PL-D-G02	Extra-pure, grade G-02	
PL-D-G01P	agglomerate free, positively charged	
PL-Nanopure-G01P	4 wt.% nanodiamonds aqueous suspension, grade G	
DNA-TAN	DNA-TAN	Special Construction-Technological Bureau «Tekhnolog», St. Petersburg, Russia
DNA-STP	DNA-STP	
UDA-S	UDA-S, ultradispersed diamond powder	The Laboratory of ultradispersed diamonds of Joint Stock Company Federal Research and Production Center ALTAI, Biysk, Russia
UDA-S-GO	UDA-S-GO, ultradipersed diamond powder of deep purification	
UDA-SP	UDA-SP, ultradispersed diamonds	JSC «SINTA», Minsk, Republic of Belarus
UDA-GO-SP	UDA-GO-SP, deep purified ultradispersed diamonds	
UDA-GO-SP-M1	UDA-GO-SP-M1, modified ultradispersed diamonds, type M1	
UDA-GO-SP-M2	UDA-GO-SP-M2, modified ultradispersed diamonds, type M2	

2.2. Instrumentation

IR spectra of nanodiamond powders were recorded on a Bruker Vertex 70 single-beam IR Fourier spectrometer (Bruker Optik GmbH, Germany) equipped with a KBr beamsplitter and a wide-range room temperature DLaTGS detector or liquid nitrogen cooled photovoltaic MCT detector. The spectrometer and accessories were continuously purged with –70°C dew point air (produced by a PG28L Purge Gas Generator, PEAK Scientific) with a flow of 500 L/h. The overall laboratory temperature was maintained at 23 ° C with an allowable variation of ± 1 °C using an air conditioner

2.2.1 PAS-FTIR

A MTEC PAC300 photoacoustic accessory (MTEC Photoacoustic, Inc, USA) and PAS-FTIR spectra were obtained by varying the scanning frequency; software correction of the peaks of CO_2 and H_2O was not used. The parameters for recording PAS-FTIR spectra are shown in Table 2. Samples of nanodiamonds were placed in a cell that was installed in the accessory, the cell compartment was purged with helium for 5–10 s. The number of scans for a sample and

Preprints (www.preprints.org) | NOT PEER-REVIEWED | Posted: 30 November 2020 doi:10.20944/preprints202011.0740.v1

background: at an interferometer frequency of 1.6 kHz, is 64, at 2.5 kHz is 128, at 5 kHz, 256. In PAS-FTIR mode, before each image, the spectrum of the background signal was recorded using highly pure compressed graphite. Samples weighing 5–10 mg were examined. For interferometer frequencies of 1.6 and 2.5 kHz, sample signal amplification modes were 1000 and 2000 times, respectively.

The resulting spectra were subjected to automatic baseline correction and 25-point smoothing.

Table 2. Parameters of recording NDs spectra in the middle IR by PAS-FTIR

Spectral range, cm^{-1}	4000-500
Resolution, cm^{-1}	4
Background scan	64; 256
Sample scan	64; 256
Phase resolution	10
Phase correction mode	Mertz
Zero filling factor	2
Apodization function	Blackman-Harris 3-Term
Aperture setting	8 mm
Interferometer frequency	1.6; 2.5; and 5 kHz
Sample and background pre-amplification gain	B (middle amplification)
Sample signal gain	Auto
Detector	microphone
Source	MIR
Beam splitter	KBr

2.2.2 ATR-FTIR

The GladiATR™ single reflection attenuated total internal reflection accessory with a diamond crystal (Pike Technologies, USA) was used for spectra registration in ATR mode. The accessory was configured for heating up to 215 °C. A background signal was recorded prior each new sample. The registration parameters of ATR spectra are shown in Table 3. Samples of nanodiamonds were transferred in a dry state to a crystal of an ATR attachment, and then clamped with a clamping screw.

Room temperature DLaTGS did not have a software-variable gain level, therefore, in all measurements, the "Ref" level was used, which means no gain in OPUS software. The Photovoltaic MCT DETECTOR had three gain levels in order of increasing gain: no gain (“Ref”), a standard (low) gain (A), and a medium gain (B).

Table 3. Parameters of recording NDs spectra in the middle IR by ATR-FTIR

Spectral range, cm^{-1}	4000–370 (with DLaTGS detecror) or 6000–700 (with MCT detector)
Resolution, cm^{-1}	2
Background scan	128
Sample scan	128
Aperture setting	8 mm
Phase resolution	4
Phase correction mode	Mertz
Zero filling factor	1
Apodization function	Blackman–Harris 3-Term
Sample and background pre-amplification gain	«Ref» (without amplification)
Background signal gain	Auto

Preprints (www.preprints.org) | NOT PEER-REVIEWED | Posted: 30 November 2020 doi:10.20944/preprints202011.0740.v1

Sample signal gain	Auto
Scanner velocity	10 kHz
Detector	Room temperature DLaTGS or liquid nitrogen cooled photovoltaic MCT
Source	MIR
Beam splitter	KBr
Background	Diamond crystal with a lowered pressure screw with a flat end

Before recording the spectra with heating, the spectrum of an empty ATR crystal was recorded at 25 °C as a background, then a small amount of the sample was placed on its surface, pressed with a screw, and a program of controlled heating was started at a rate of 0.25 °C/min from 25 °C to 215 °C, and spectra registration step every 2.5 °C. After heating to 215 ° C and recording the spectrum, the sample was cooled to 25 °C. The resulting array of heating spectra (25–215 ° C) was combined, and then a similar array of spectra of an empty ATR crystal was subtracted from it

2.2.3 DRIFT

The PrayingMantis™ diffuse reflection accessory (Harrick Scientific Products, INC.) was used for spectra registration in diffuse reflectance mode. The registration parameters of DRIFT spectra are shown in Table 4.

Table 4. Parameters of recording ND spectra in the near to middle IR by DRIFT

Spectral range, cm^{-1}	7000–400
Resolution, cm^{-1}	2
Background scan	256
Sample scan	256
Phase resolution	16
Phase correction mode	Mertz
Zero filling factor	2
Apodization function	Blackman–Harris 3-Term
Aperture setting	3 mm
Sample and background pre-amplification gain	«Ref» (without amplification) for DLaTGS detector A (standard amplification) for MCT detector
Background signal gain	Auto
Sample signal gain	Auto
Scanner velocity	10 kHz
Detector	Room temperature DLaTGS or liquid nitrogen cooled photovoltaic MCT
Source	MIR
Beam splitter	KBr
Background	Mirror

Software automatically converted spectra measured in diffuse reflectance using the Kubelka–Munk (KM) conversion. The conversion is based on the following formula:

$$KM = \frac{(1 - Refl)^2}{(2 \times Refl)}$$

where Refl is the relation between reflected and incident light. Absorbance spectra are first converted to transmittance spectra. The smallest value allowed for transmittance or reflectance is 0.001%. This equals a Kubelka Munk value of about 500.

For background measurements the tilted alignment mirror for PrayingMantis™ accessory was used. For this the alignment fixture was slide into the accessory, with the horizontal mirror going in first. In this orientation, the tilted mirror is in the sampling position. We compare this approach with KBr in sample cup.

Preprints (www.preprints.org) | NOT PEER-REVIEWED | Posted: 30 November 2020 doi:10.20944/preprints202011.0740.v1

2.2 Data Handling

All spectra were processed in the Bruker OPUS 7.5 software. PAS-FTIR spectra were smoothed out by 25 points, DRIFT and ATR-FTIR by 13 points (at some figures spectra are presented without smoothing).

The penetration depth of damped IR radiation with the wavenumber $\tilde{\nu}$ into the sample approaching the ATR crystal/sample boundary at an angle θ to the normal) was estimated as:

$$\mu_{ATR}(\tilde{\nu}) = \left(2\pi\tilde{\nu}n_{ATR}\sqrt{(\sin\theta^2 - (n_{ATR}/n_S)^2)}\right)^{-1}, (1)$$

where n_{ATR} and n_S are refractive indexes of the ATR crystal and sample, respectively.

In PAS-FTIR, the estimation of the radiation penetration depth is made using the dependence of the penetration depth of the heat wave

$$\mu_{PAS}(\tilde{\nu}) = \sqrt{D_T/2\pi V\tilde{\nu}}, (2)$$

where D_T is the thermal diffusivity of the sample and V is the interferometer mirror velocity [33]. Thermal diffusivity D_T was taken as 7.8 cm²/s [34], the velocities of the difference in optical paths of the IR spectrometer were obtained from the interferometer modulation frequencies and the He–Ne laser reference line: 0.1012 and 0.1582 cm/s, respectively.

2.3 Procedures

The PAS-FTIR spectra obtained by method 3 with an interferometer frequency of 1.6 kHz and an amplification of the signal of sample 1000 were smoothed over 25 points and the intensity was multiplied by $\sqrt{\tilde{\nu}}$ [33]. The ATR spectra were additionally transformed as follows: $I_0a + b = I_{corr}$, where I_0 is the intensity of the ATR spectra after the operations described above, I_{corr} is the intensity of the ATR spectra for comparison with the PAS-FTIR spectra, $a = 150$, $b = 1$.

2.3.1 Reproducibility

To compare reproducibility, ten ATR-IR spectra of nanodiamonds were recorded with re-registration of the background spectrum after each measurement due to the high abrasive ability of nanodiamonds. After registration, the spectra were not subjected to extended ATR correction. Baseline correction and anti-aliasing were not applied.

10 PAS-FTIR spectra were recorded according to method 3 with a complete overfilling of the sample cup and an interferometer frequency of 1.6 kHz. PAS-FTIR spectra were not subjected to automatic baseline correction and smoothing. RSD and signal-to-noise ratio ($S/N = 1/RSD$) were calculated as

$$RSD = \sqrt{\frac{\sum_i (x_i - \bar{x})^2}{n-1}}\frac{1}{\bar{x}} (3)$$

3. Results

3.1. Band assignment

The spectra of nanodiamonds for the studied brands are shown in Figs. 1–3 for DRIFT, Figs. 4–6 for ATR, and Fig. 7 for FTIR-PAS. All the assigned bands existing in spectra of all the selected ND brands are summed up in Table 5. In this section, we describe the assignment of all major bands present in most brands in at least two modalities and all the measurement conditions; the comparison and differences in spectra for IR modalities and specific features of brands are given in the next section.

Preprints (www.preprints.org) | NOT PEER-REVIEWED | Posted: 30 November 2020 doi:10.20944/preprints202011.0740.v1

Table 5. The assignment of major bands common to most ND brands [16, 35-41]

Wavenumber	Assignment	ATR	DRIFT	PAS*
5900–5600	2ν C–H aliphatic chain stretching	—	W	—
5300	Water combination band $av_1 + v_2 + bv_3$; $a + b = 1$	—	Mb	Wb
4800	Aromatic C–H combination bands (?)**	—	Wb	—
4500–4100	Aliphatic C–H combination bands	—	Wb To Mb	W
3715	Hydrogen-bonded –O–H···H–O– stretch	—	Wp	Wp
3695	Hydrogen-bonded –O–H···H_2O stretch	—	Mp	Wp (noisy)
3569	Hydrogen-bonded RO–H…H_2O H–OR stretch (?)	—	W	W (noisy)
3450–3420	Liquid: antisynchronous stretch v_3	Mv	Sv	Mv
3407	O–H stretch and intermolecular hydrogen bonds (unresolved)	Mb to Wb	—	Mb to Wb
3290	H–O–H bend of liquid adsorbed water, $2v_2$	—	Wv	W
3230–3210	Liquid: synchronous stretch, v_1	Sv	Sv	Sv
3050	Aromatic C–H stretching	W to none	S	M
2970	Alkene C–H stretch	W to none	M	W
2950–2940	Aliphatic C–H, CH_3 antisymmetric stretch	W to none	S	M
2940–2930	Aliphatic C–H, CH_2 antisymmetric stretch	—	S	S
2880–2870	Aliphatic C–H, CH_3 symmetric stretch	W to none	S	M
2850–2835	Aliphatic C–H, CH_2 symmetric stretch	W to none	Wb	M
2750–2550	Carboxylic O–H stretch	Wb to none	Mb to Wb	Wb to none*
2150	Water combination band $v_2 + L_2$	Wb	Wb	Wb
1800–1780	C=O stretch of conjugated carboxyl groups	M	S	S to M*
1765–1730	C=O stretch of monomeric carboxyl groups	Mb	Sb	Sb to Mb*
1670	C=O stretch of non-carboxyl carbonyl (?) C=C stretch	W	W	M
1644–1642	H–O–H bend of liquid water, v_2	Sv	Mv	Mv
1630–1625	H–O–H bend of adsorbed liquid water, v_2	Sv	Mv	Mv
1610	H–O–H bend of adsorbed liquid water, v_2	Ssh	Msh	Msh
1580–1560	adsorbed water C=C stretch, (?)	M	M	M
1470–1450	sp^3 CH_2 wagging	S	M	
1440	Carboxyl C–O–H in-plane bend Aromatic, ring C=C stretch	—	Wb	W
1410	Carboxyl C–O–H in-plane bend	Msh	Msh	Msh
1400–1395	Non-carboxyl C–O–H in-plane bend CH_2 deformation (scissors)	Msh	Ssh	Ssh
1373	Non-carboxyl C–O–H in-plane bend CH_3 deformation (umbrella)	M	Ssh	M
1330	Non-carboxyl C–O–H in-plane bend (?)	S	M	S to M*
1270–1267	Carboxyl C–O stretch	W	M	M
1245–1235	C–N stretch	W	W	W

Preprints (www.preprints.org) | NOT PEER-REVIEWED | Posted: 30 November 2020 doi:10.20944/preprints202011.0740.v1

1192	C–C–C (?)	—	M	W
1145–1130	C–O–C (?)	—	M	W
1103	Non-carboxyl C–O stretch	Sb	Sb	Sb
1060–1040	In plane –C–H bend (non-aromatic) and carbohydrates (?)	W	Wsh	Wb
1000–500	Water librations, L_2,	Sb	Sb	Mb to Wb
960–940	Carboxyl out-of-plane C–O–H bend, $=CH_2$ wagging (?)	M	Wb	M to W*
830	Aromatic =C–H bend	Mp	Mp	Mp
760	Polyaromatic =C–H bend (?)	—	W	M to none*
610	Non-carboxyl out-of-plane C–O–H bend	W	M	Wb to none*
410	(?) C–C in-phase vibrations	M	Wb	—

Notation: S = strong; M = medium; W = weak; p = peak (sharp); b = broad; v = variable; sh = shoulder.

* Intensity depends on the modulation frequency (PAS); ** (?) not fully clear.

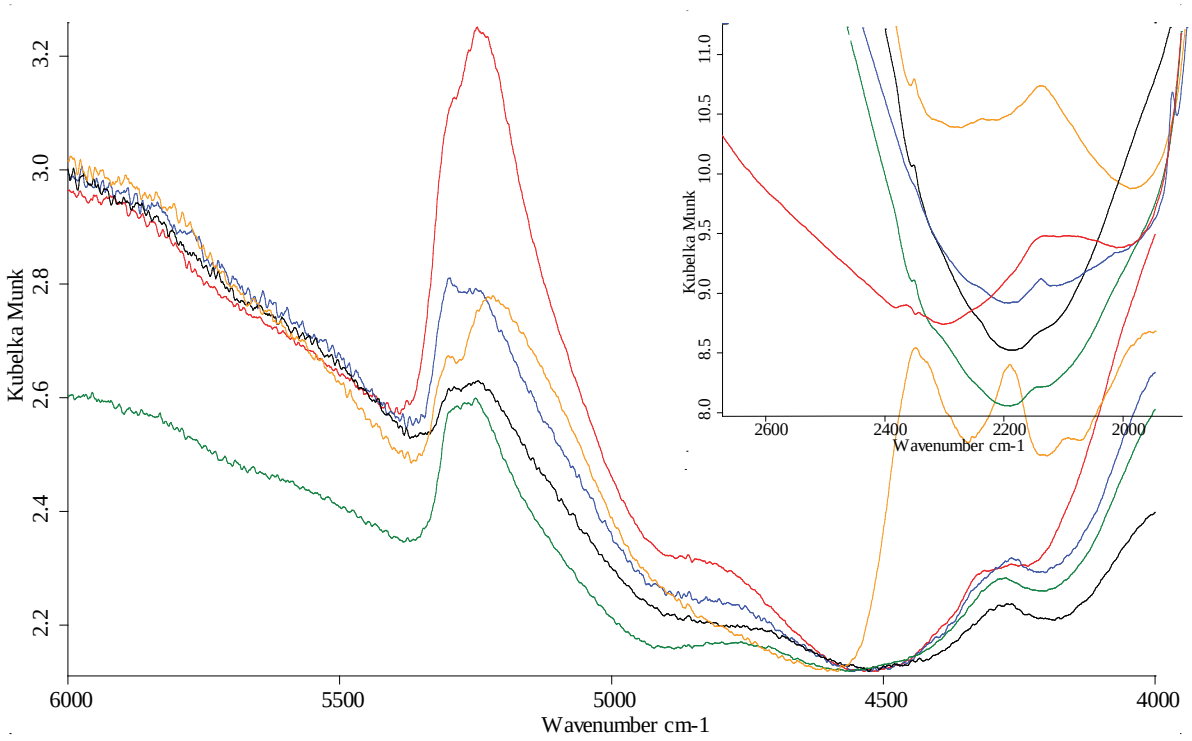

(a)

Preprints (www.preprints.org) | NOT PEER-REVIEWED | Posted: 30 November 2020 doi:10.20944/preprints202011.0740.v1

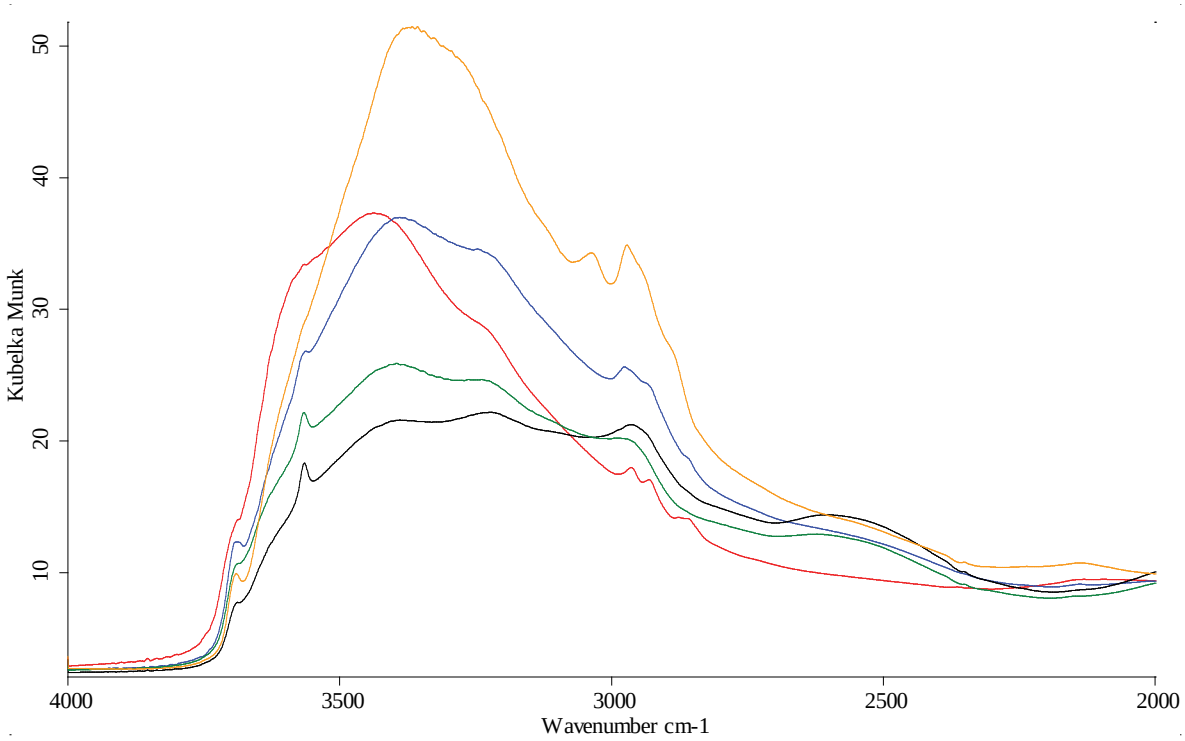

(b)

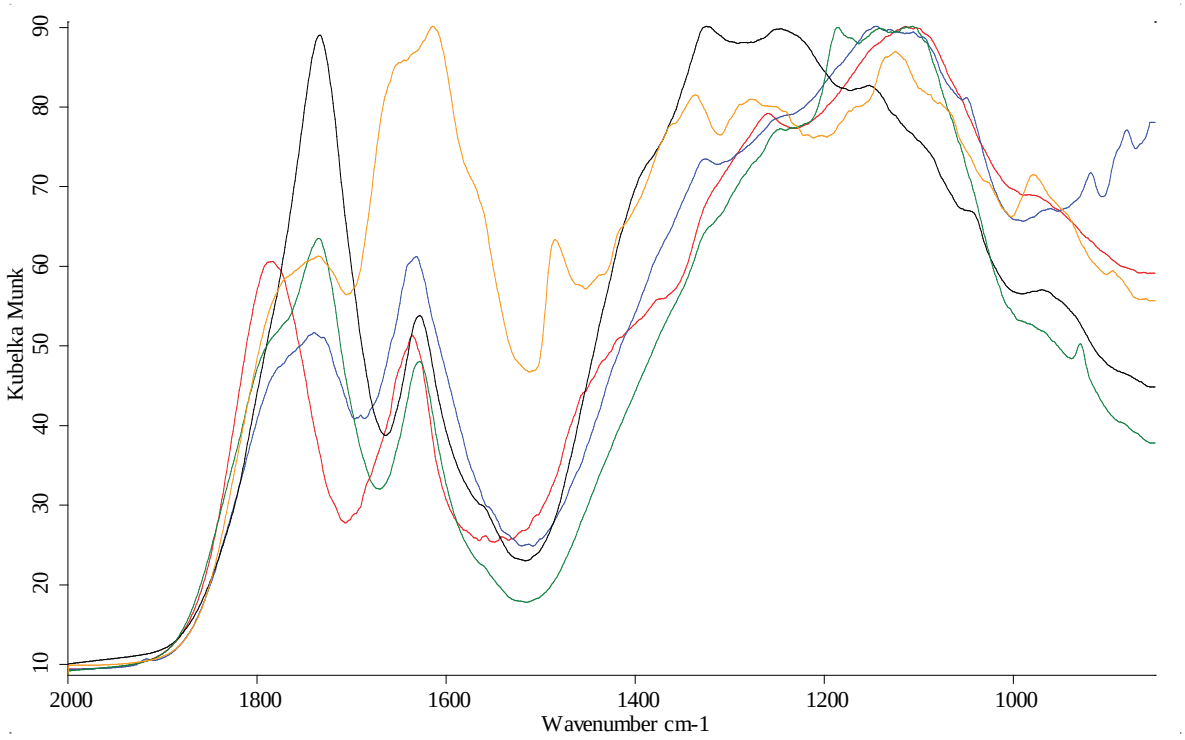

(c)

Figure 1. Diffuse reflectance mode, LN-MCT photovoltaic detector, red –SDND, blue – PL-Nanopure GO1, black – PL-D-G, green – PL-D-G02, orange- PL-D-G01P **(a)** 6000–4000 cm^{-1}, **(b)** 4000–2000 cm^{-1} (c) 2000–800 cm^{-1} range. Spectra were smoothed (13 points) and normalized to maximize each spectrum.

Preprints (www.preprints.org) | NOT PEER-REVIEWED | Posted: 30 November 2020 doi:10.20944/preprints202011.0740.v1

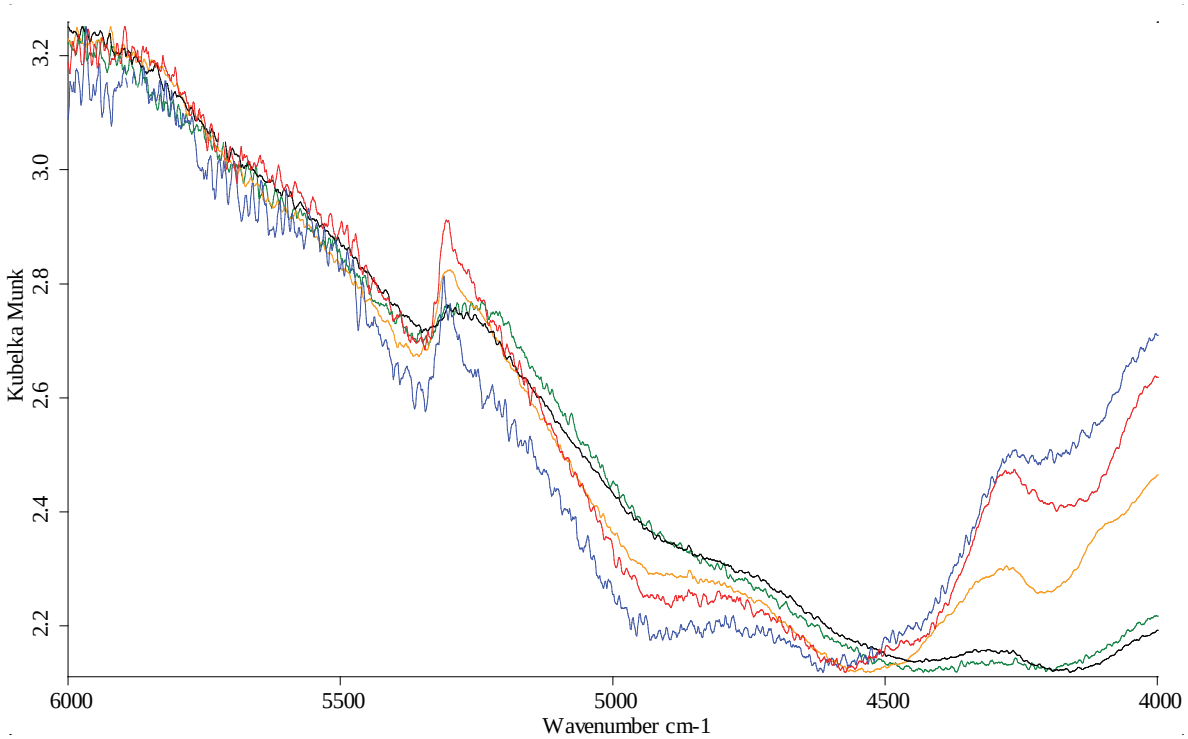

(a)

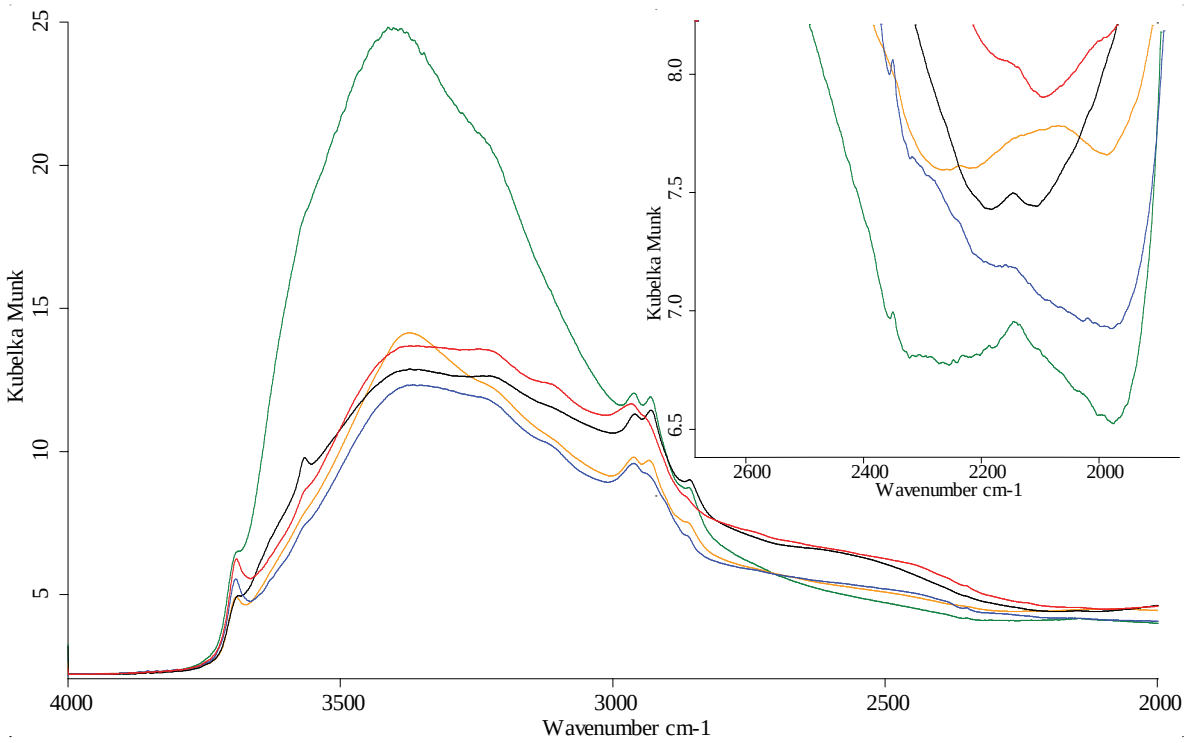

(b)

Preprints (www.preprints.org) | NOT PEER-REVIEWED | Posted: 30 November 2020 doi:10.20944/preprints202011.0740.v1

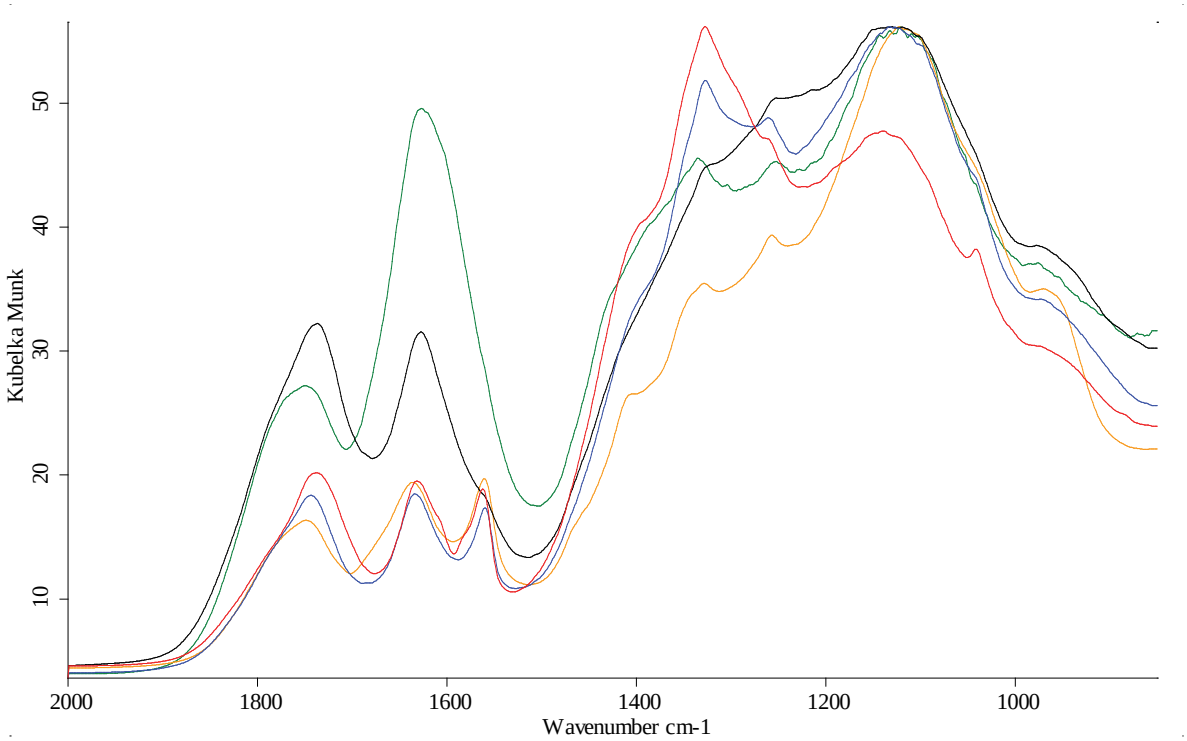

(c)

Figure 2. Diffuse reflectance mode, LN-MCT photovoltaic detector, red –DNA-STP, blue – DNA-TAN, black – UDA-S-GO, green – UDA-S, orange- UDA-SP **(a)** 6000–4000 cm^{-1}, **(b)** 4000–2000 cm^{-1} (c) 2000–800 cm^{-1} range. Spectra were smoothed (13 points) and normalized to maximize each spectrum.

Preprints (www.preprints.org) | NOT PEER-REVIEWED | Posted: 30 November 2020 doi:10.20944/preprints202011.0740.v1

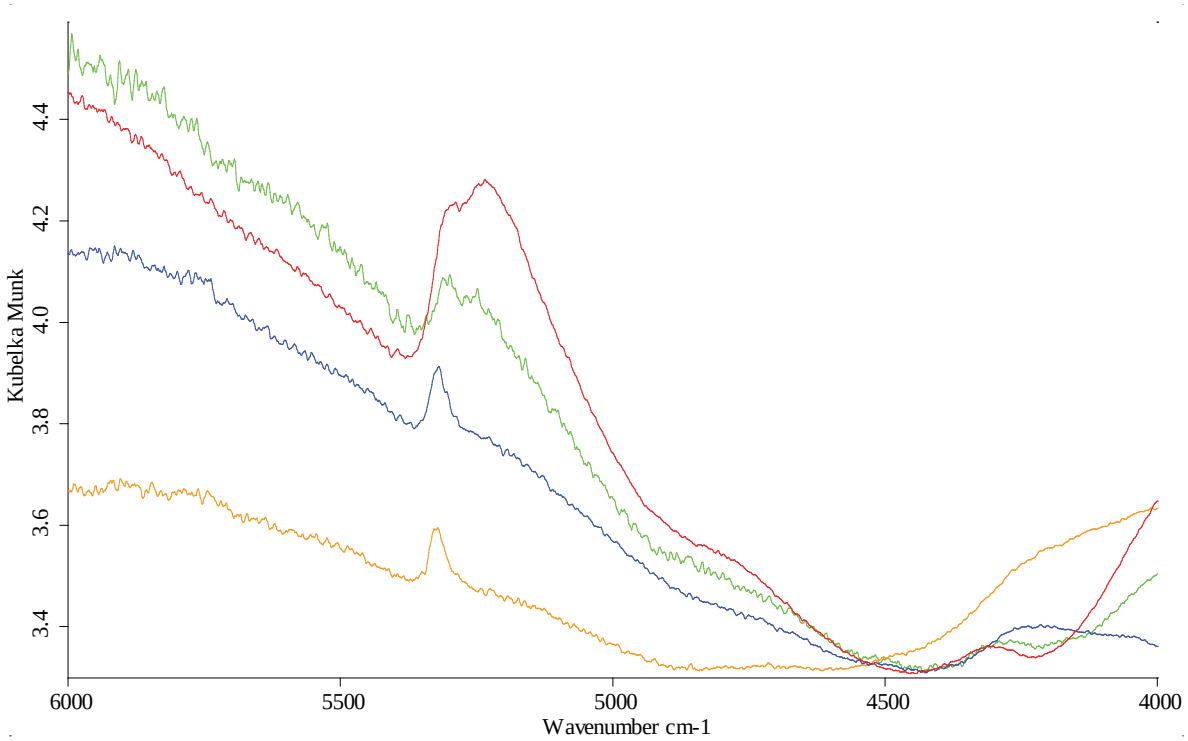

(a)

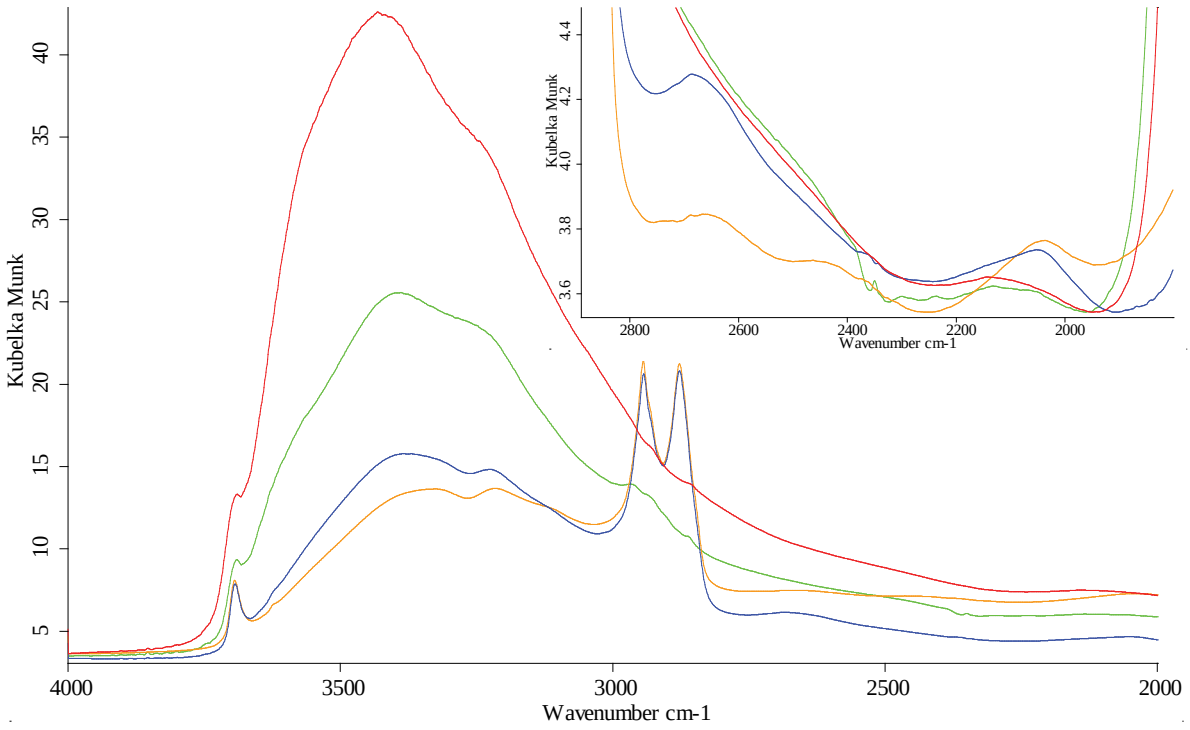

(b)

Preprints (www.preprints.org) | NOT PEER-REVIEWED | Posted: 30 November 2020 doi:10.20944/preprints202011.0740.v1

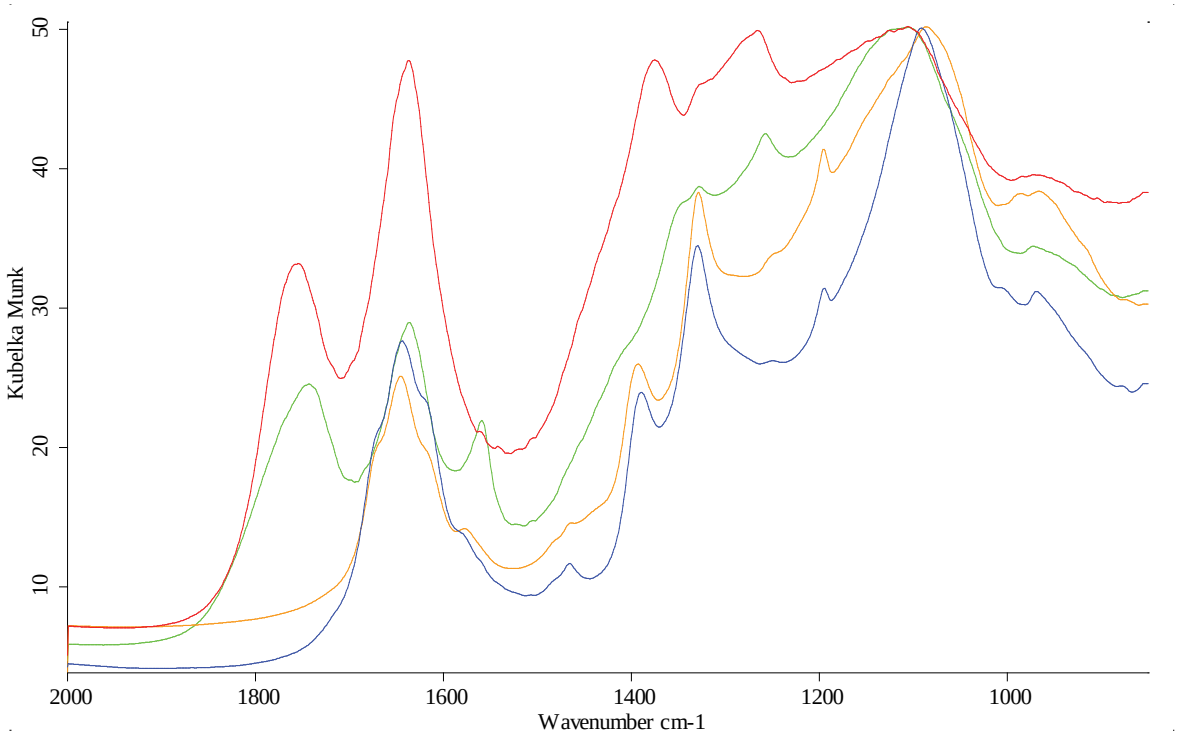

(c)

Figure 3. Diffuse reflectance mode, LN-MCT photovoltaic detector, red –RUDDM, blue – UDA-GO-SP-M1, orange- UDA-GO-SP-M2, green – UDA-GO-SP **(a)** 6000–4000 cm^{-1}, **(b)** 4000–2000 cm^{-1} (c) 2000–800 cm^{-1} range. Spectra were smoothed (13 points) and normalized to maximize each spectrum.

Preprints (www.preprints.org) | NOT PEER-REVIEWED | Posted: 30 November 2020 doi:10.20944/preprints202011.0740.v1

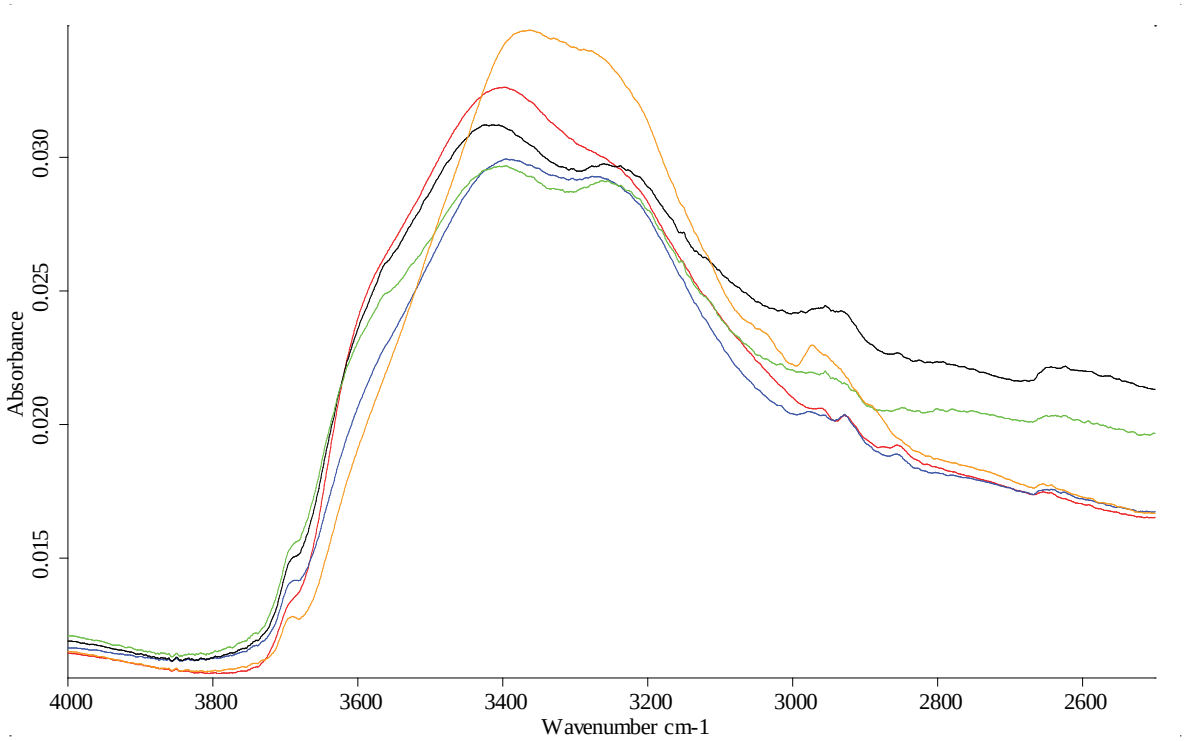

(a)

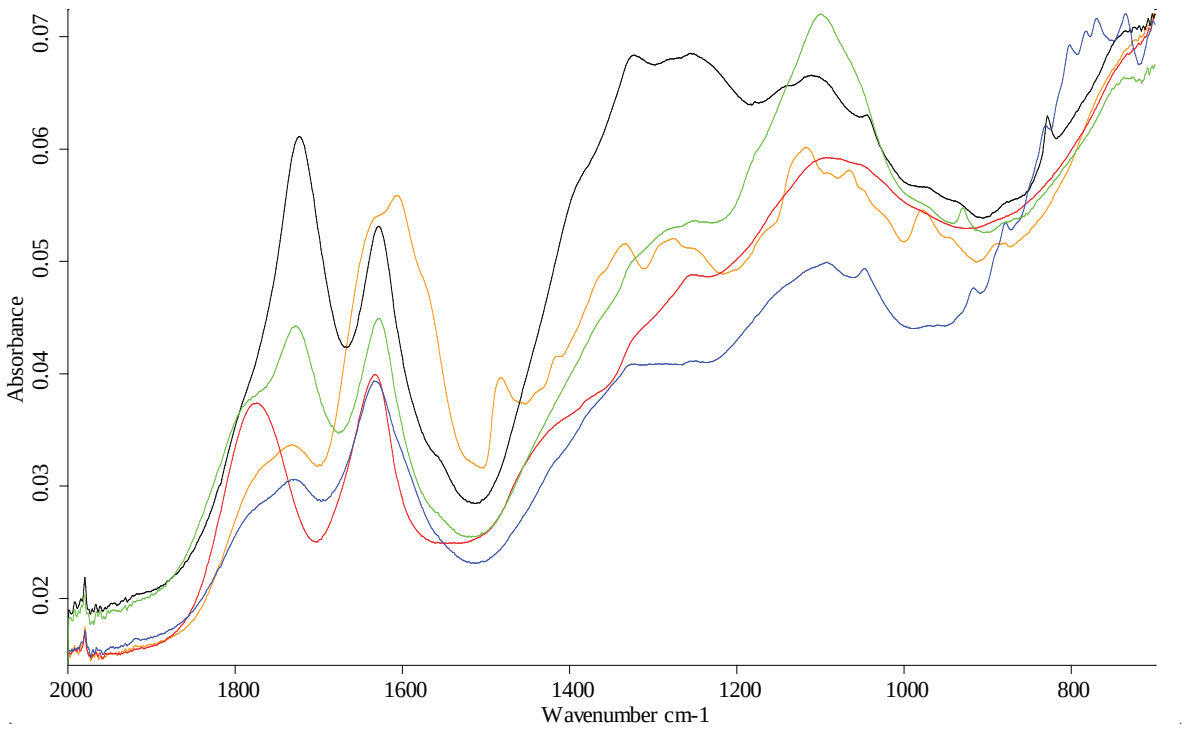

(b)

Figure 4. ATR mode, LN-MCT photovoltaic detector, red –SDND, blue – PL-Nanopure GO1, black – PL-D-G, green – PL-D-G02, orange- PL-D-G01P **(a)** 4000–2500 cm^{-1}, **(b)** 2000–400 cm^{-1} range. Spectra were smoothed (13 points) and normalized to maximize each spectrum.

Preprints (www.preprints.org) | NOT PEER-REVIEWED | Posted: 30 November 2020 doi:10.20944/preprints202011.0740.v1

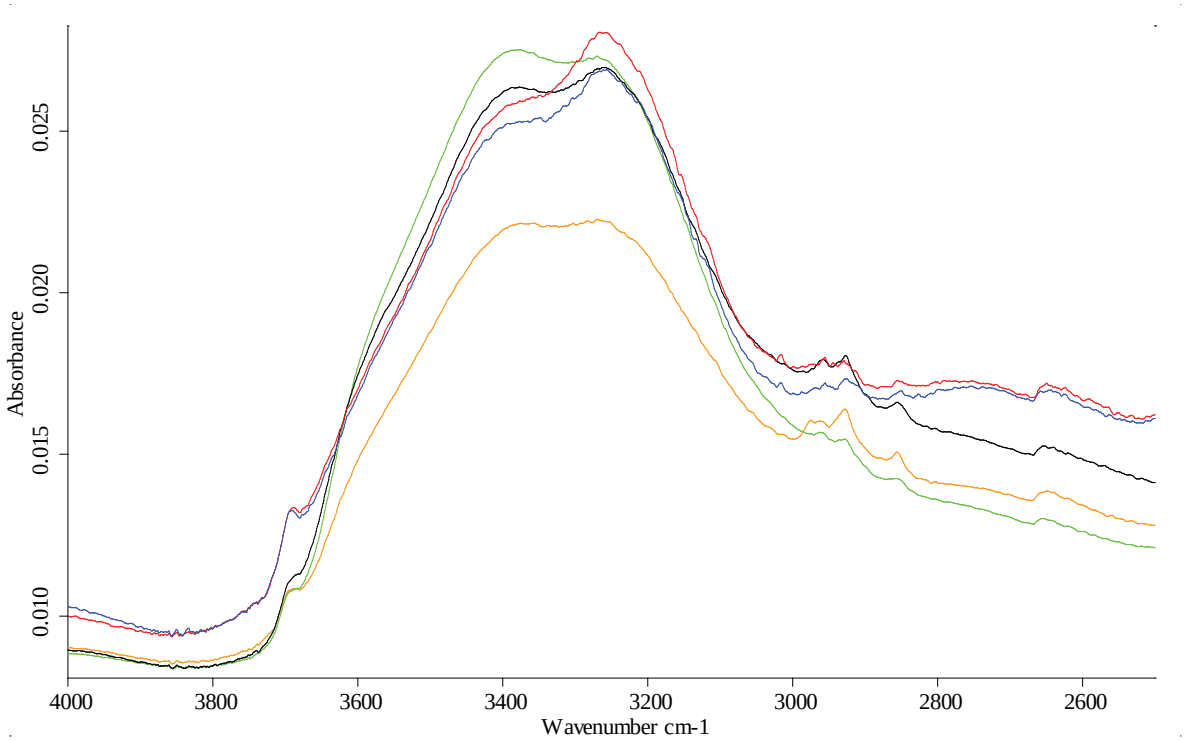

(a)

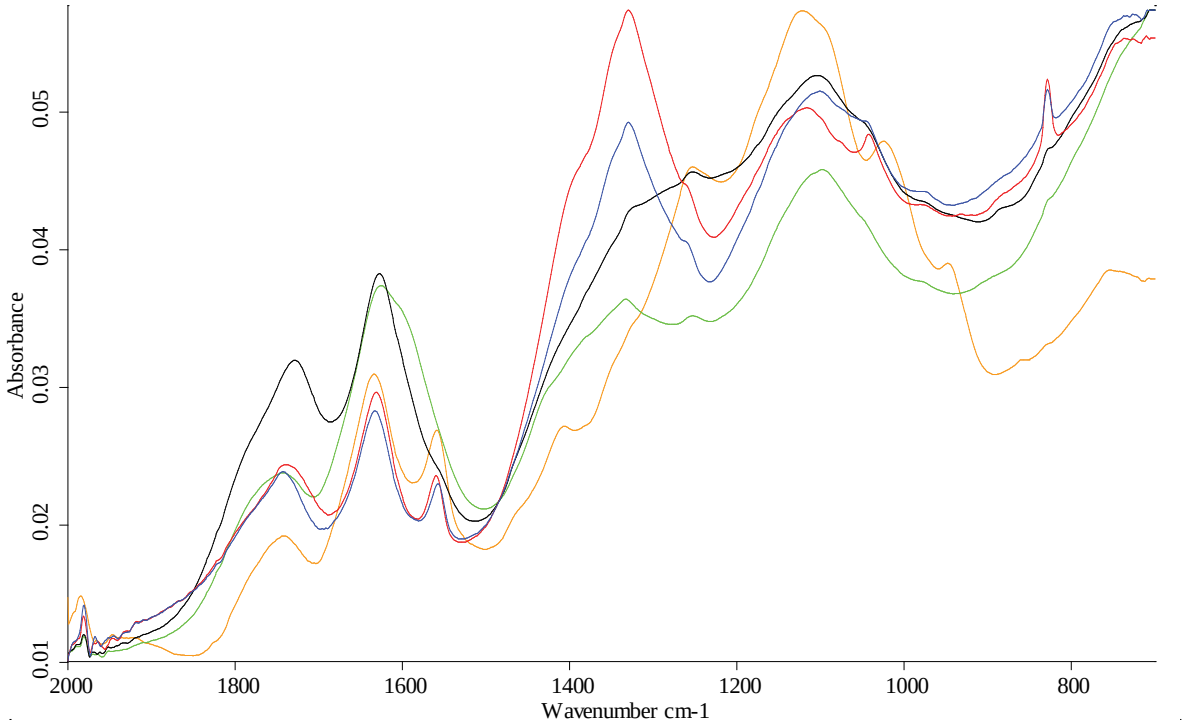

(b)

Figure 5. ATR mode, LN-MCT photovoltaic detector, red –DNA-STP, blue – DNA-TAN, black – UDA-S-GO, green – UDA-S, orange- UDA-SP **(a)** 4000–2500 cm^{-1}, **(b)** 2000–400 cm^{-1} range. Spectra were smoothed (13 points) and normalized to maximize each spectrum.

Preprints (www.preprints.org) | NOT PEER-REVIEWED | Posted: 30 November 2020 doi:10.20944/preprints202011.0740.v1

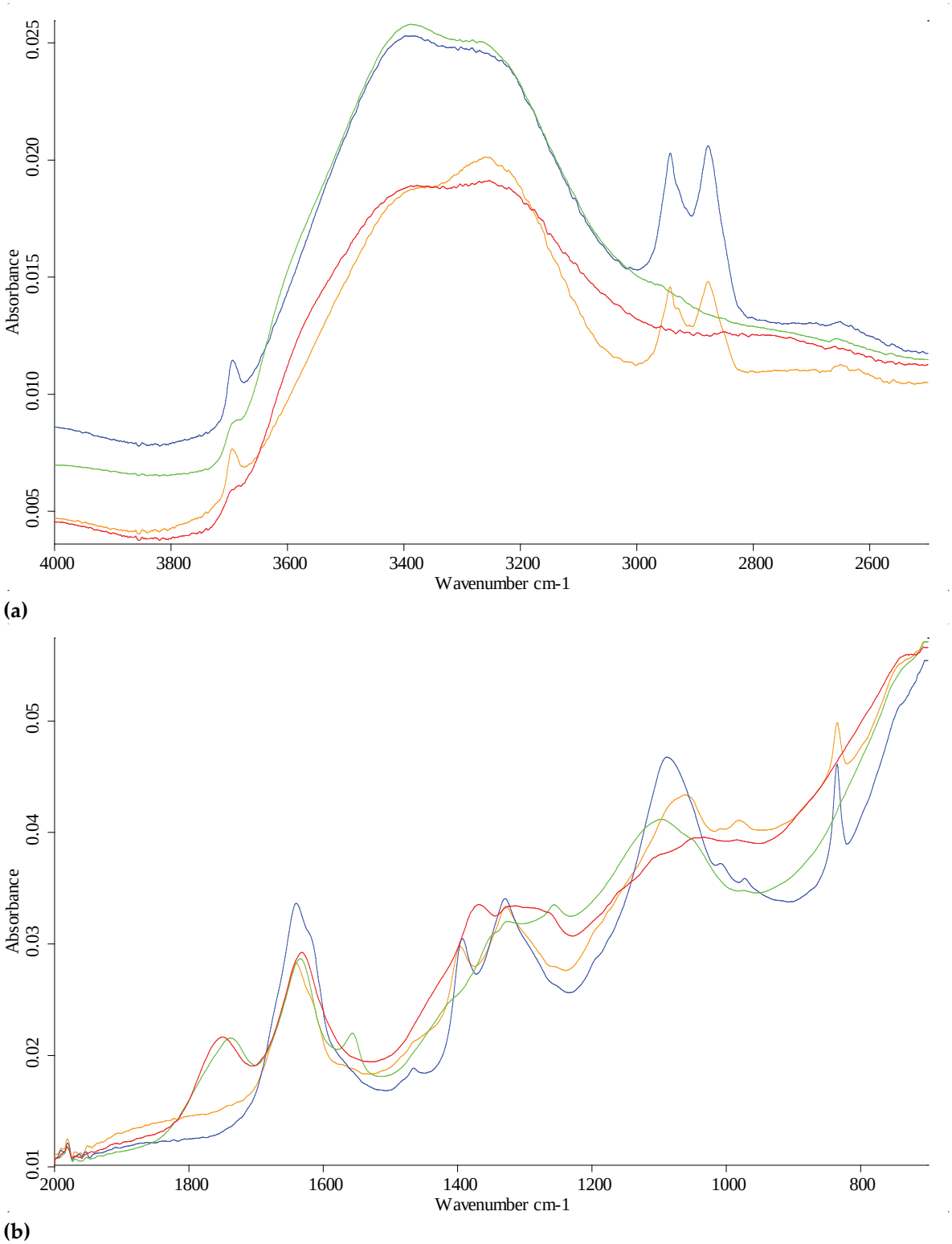

Figure 6. ATR mode, LN-MCT photovoltaic detector, red –RUDDM, blue – UDA-GO-SP-M1, orange-UDA-GO-SP-M2, green – UDA-GO-SP **(a)** 4000–2500 cm^{-1}, **(b)** 2000–400 cm^{-1} range. Spectra were smoothed (13 points) and normalized to maximize each spectrum.

Preprints (www.preprints.org) | NOT PEER-REVIEWED | Posted: 30 November 2020 doi:10.20944/preprints202011.0740.v1

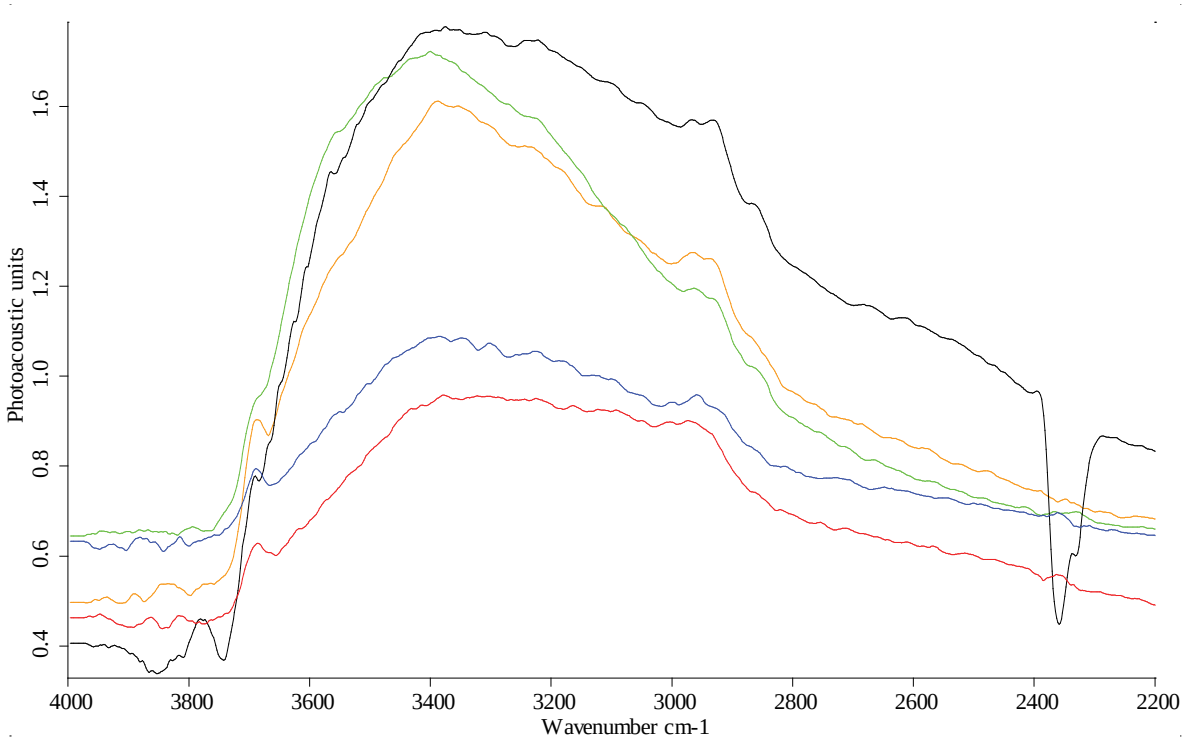

(a)

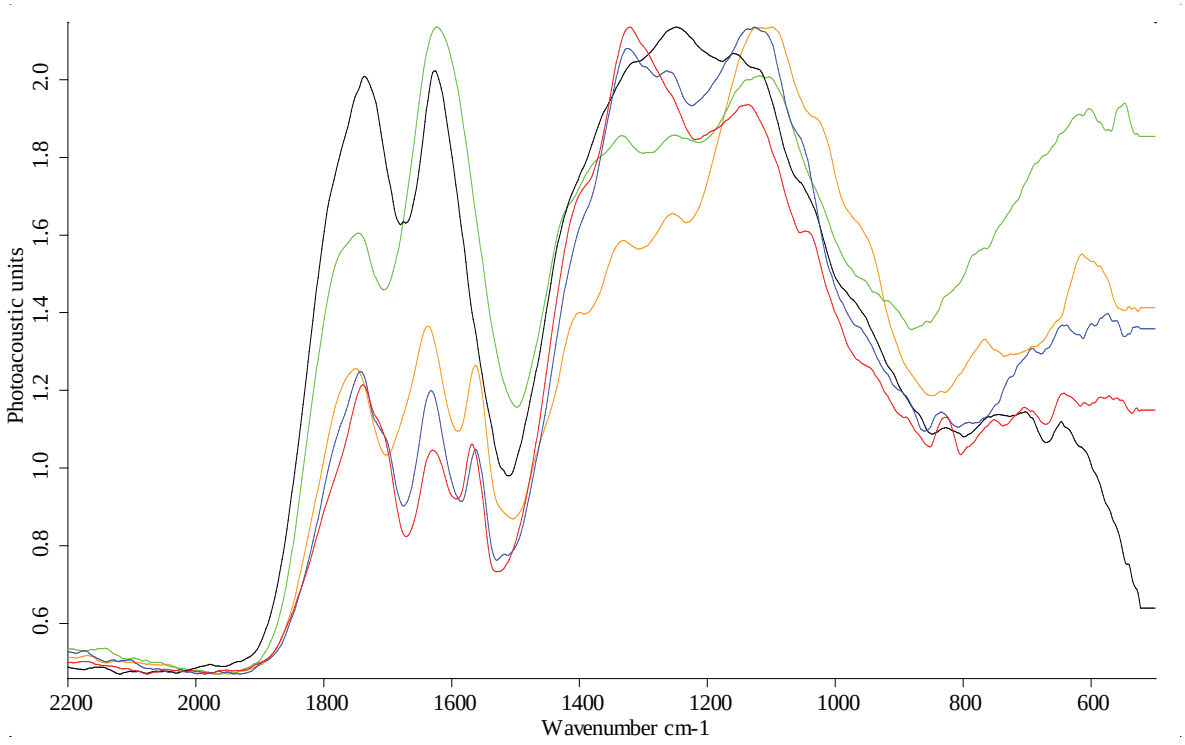

(b)

Figure 7. Optoacoustic mode, red –DNA-STP, blue – DNA-TAN, black – UDA-S-GO, green – UDA-S, orange- UDA-SP **(a)** 4000–2200 cm^{-1}, **(b)** 2200–400 cm^{-1} range. Spectra were smoothed (25 points) and normalized to maximize each spectrum.

The near IR region shows two wide bands at 5900–5600 and 4300 cm^{-1} that are C–H first overtone and combination bands, respectively (Fig. 1A). In some cases, a weak broad band at 4800 cm^{-1} that may be attributed to aromatic C–H combination bands is present. They are revealed by DRIFT and PAS-FTIR and not ATR. Also, these modalities show a rather explicit combination band

Preprints (www.preprints.org) | NOT PEER-REVIEWED | Posted: 30 November 2020 doi:10.20944/preprints202011.0740.v1

of water at 5300 cm^{-1} with intensities correlated with the intensities of water bands in the Mid-IR range.

In shortwave Mid-IR region, a wide band of 3700–3000 cm^{-1} of O–H stretch and intermolecular hydrogen bonds [36] and, at its shoulder, sharp bands at 3695 cm^{-1} of isolated water and 3569 cm^{-1} attributed to hydrogen-bon bonded water and non-water –OH groups are observed [35, 36, 42]. These bands are present in DRIFT and PAS-FTIR and are not reliably detected with ATR (Figs 4–6. Some brands show another sharp band at 3715 cm^{-1} that can be attributed to ROH…HOR hydrogen bonds.

Bands of O–H stretching vibrations (3500–3200 cm^{-1}) are present in all the spectra, and the shape depends on the modality and ND brand, the maxima of asymmetric and symmetric bands at 3410 and 3230 cm^{-1} correspond to strongly hydrogen-bonded species, and in several cases, the band at 3290 cm^{-1}, which is probably the overtone band of liquid adsorbed water, $2\nu_2$ is present [16].

All four asymmetric and antisymmetric aliphatic vibrations of sp^3 CH_x stretch vibrations in the range 3100–2800 cm^{-1} are observed in most brands, ATR shows low sensitivity (Table 5). The band at 1470 cm^{-1} corresponds to CH_2 wagging and correlates with the intensity of CH_x stretch at 2900 cm^{-1} range. Bands at 1400–1395 and 1375–1370 cm^{-1} can be attributed as CH_2/CH_3 deformation bends as well as C–O–H bends (see below), so their intensities are not correlated with purely CH_x bands at 3100–2800 cm^{-1}.

Apart from aliphatic bands, some brands show aromatic C–H stretching at 3100–3050 cm^{-1} [43] and the band at 1580–1560 cm^{-1} (most probably, C=C stretch). These bands are accompanied with distinct bands at 1060 and 760 cm^{-1} that can be attributed to in plane C=C–H and polyaromatic C=C–H bending, respectively. Also a band of 410 cm^{-1} is attributed to C–C in-phase vibrations [41]. A band at 960 cm^{-1} can be attributed to =CH_2 wag.

The range of 1900–1200 cm^{-1} reveals the maximum number of bands. Here, the stretch of the carbonyl C=O (1770–1650 cm^{-1}) is dominant, usually in the form of a continuum from 2000 to 1600 cm^{-1}; bands at 1760–1740 cm^{-1} attributed to the carbonyl of carboxylic groups and less strong bands (for not all the brands) at 1670 cm^{-1} attributed to the C=O stretch of non-carboxyl moieties are dominant (Fig. 8). There is also a weak band of 1550 cm^{-1} also belonging to asymmetric C=O stretching vibrations [36, 44] or asymmetric stretching vibrations of deprotonated carboxyl O–C=O [44, 45]; however, the comparison of the blank in PAS, ATR, and DRIFT shows that such low-intensity bands in the range 1600–1400 cm^{-1} are mostly envelope bands of gaseous water. In the case of DRIFT and ATR they are positive, but in the case of PAS these peaks are inverted and in the case of low-intensity signals can be wrongly interpreted as the broader bands red-shifted compared to other modalities (Fig. 8). The band intensities at 1700 cm^{-1} correlate well with the signal from a weak broad band 2700–2600 cm^{-1}, which is attributed to O–H stretch in carboxyl, which is red-shifted O–H compared to the main continuum of 3500–3200 cm^{-1}. The presence of this band can be considered as a proof of carboxylic groups at the surface.

Preprints (www.preprints.org) | NOT PEER-REVIEWED | Posted: 30 November 2020 doi:10.20944/preprints202011.0740.v1

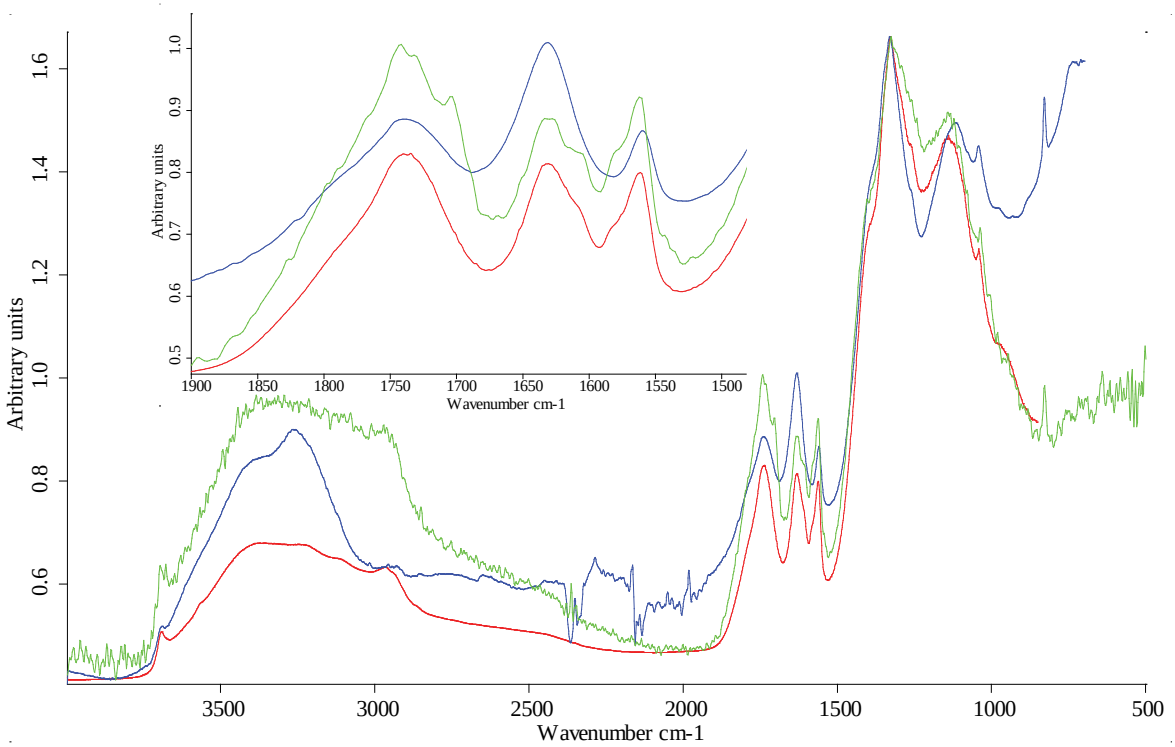

Figure 8. UDA-STP nanodiamonds, red –ATR mode with photovoltaic MCT detector, blue – diffuse reflectance mode with photovoltaic MCT detector, green – photoacoustic mode. Spectra weren't smoothed but normalized to maximize each spectrum.

A band of H–O–H bending vibrations of liquid unbound or loosely bound water 1643 cm^{-1} is present in all the spectra; all the studied air-dried samples contain 5–7% of water [46, 47]. Another band of water (1620–1635 cm^{-1}) is present in all the spectra. Its wavenumber is red-shifted compared to liquid water (1643 cm^{-1}) evidencing a high contribution of hydrogen-bonding to this vibrations [48]. Its intensity decreases after drying, but this band does not disappear even after five hours of drying (Figs. 9 and 10). The presence of this band is an evidence of the water layer at the surface of nanodiamonds that determines the colloidal solubility of nanodiamonds and its division into 'soluble' and 'insoluble' brands [5].

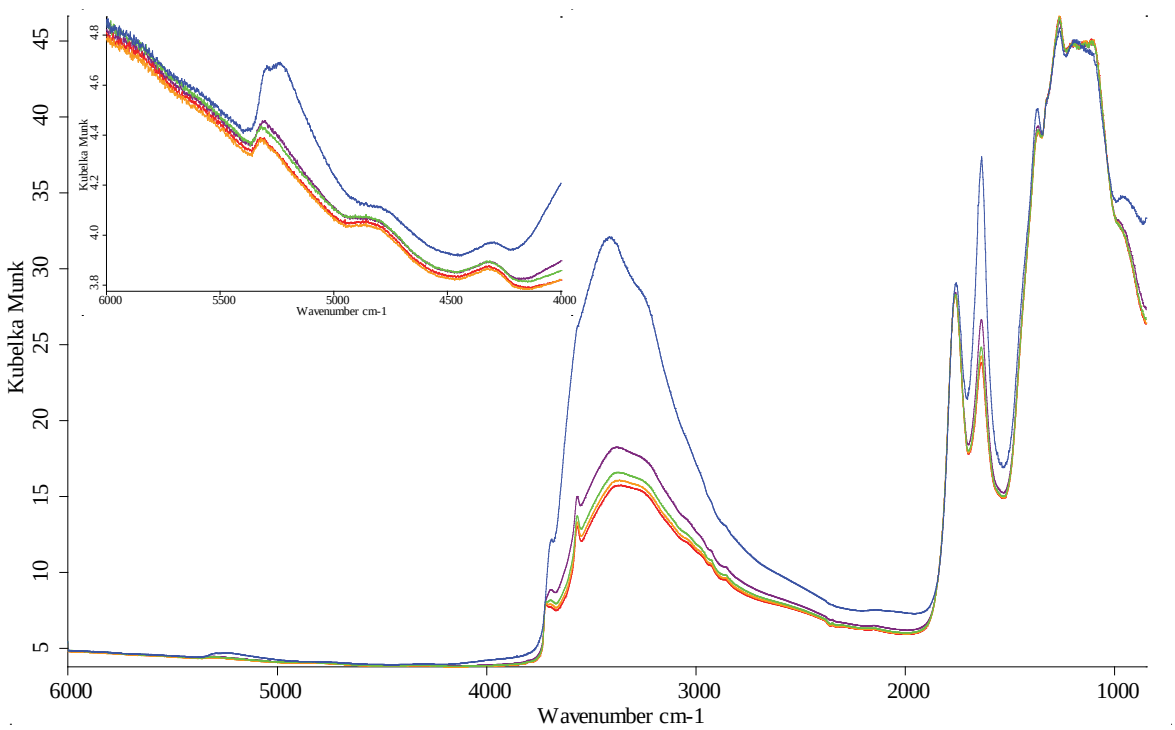

Preprints (www.preprints.org) | NOT PEER-REVIEWED | Posted: 30 November 2020 doi:10.20944/preprints202011.0740.v1

Figure 9. RUDDM nanodiamonds, DRIFT with MCT, blue – immediately after sample was placed into accessory, purple – after 1 hour of purging sample inside accessory, green – 2 hours, orange – 3 hours, red – 5 hours. Spectra were not smoothed and normalized.

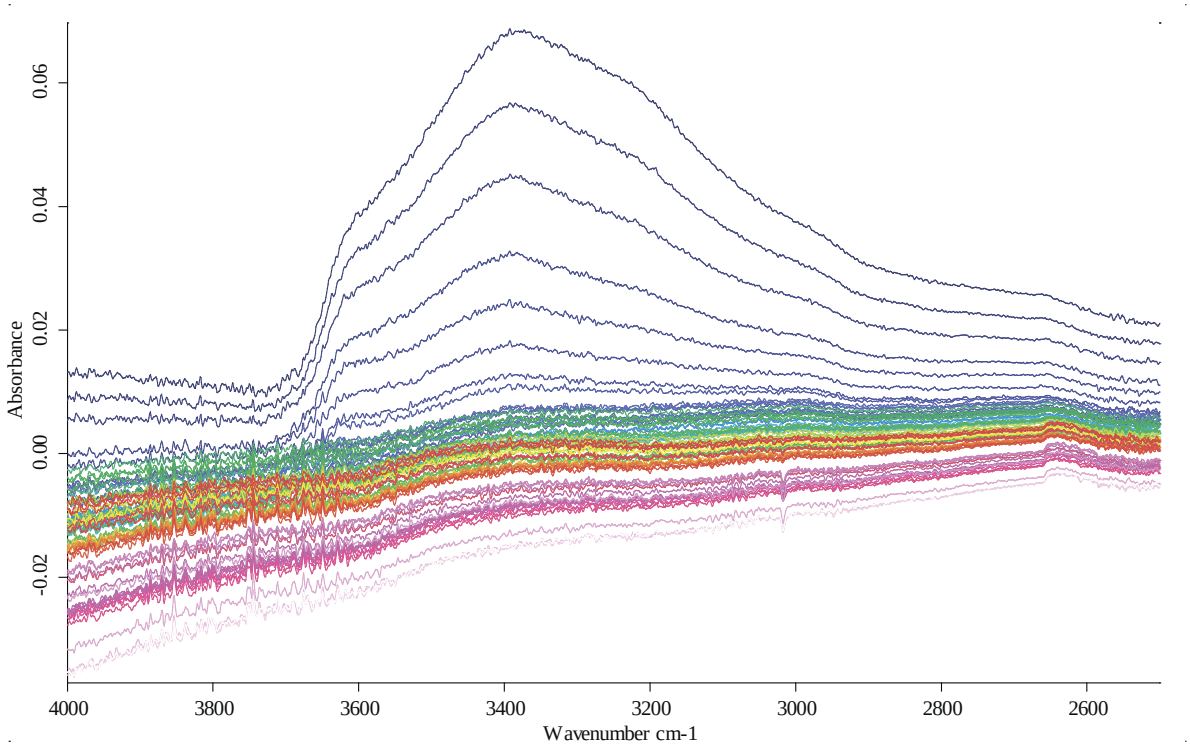

(a)

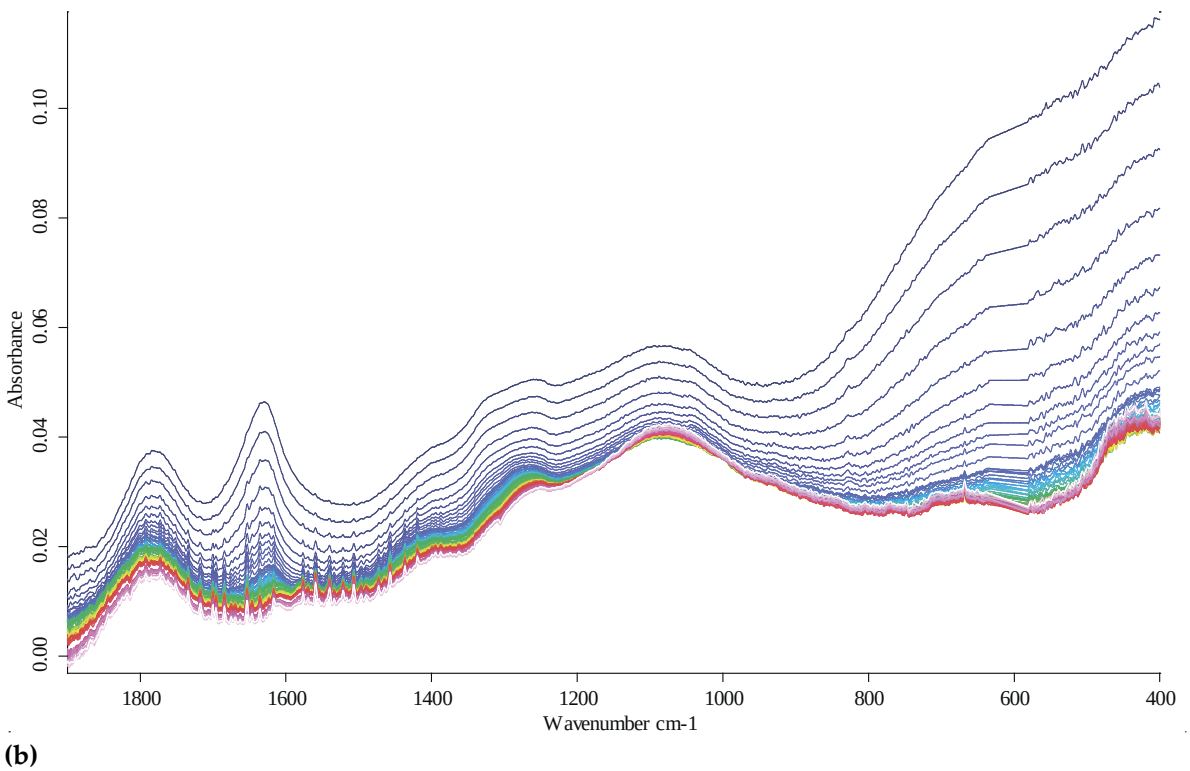

(b)

Figure 10. ATR mode, SDND nanodiamonds, heating from 25 °C (blue) to 215 °C (pink) **(a)** 4000–2500 cm^{-1}, **(b)** 2000–400 cm^{-1} range. Spectra are not smoothed.

Preprints (www.preprints.org) | NOT PEER-REVIEWED | Posted: 30 November 2020 doi:10.20944/preprints202011.0740.v1

Symmetrical bands at 1440 and 1390–1320 cm^{-1} at least partly can be assigned to C–O–H in-plane bend for carboxyl [38, 44, 45] and non-carboxyl groups [39]. The bands at 1270 cm^{-1} correspond to carboxyl C–O stretch or bending vibrations of epoxy C–O [36, 44, 45]. Weakly pronounced asymmetric bending vibrations that can be assigned to C–O–C are observed in the range of 1150–1110 cm^{-1} [36, 44, 45]. The band at 1100–1040 cm^{-1} can be attributed to non-carboxyl C–O stretch or asymmetric bending vibrations of C–O–C [36, 43-45, 49] and carboxyl and non-carboxyl out-of-plane C–O–H bend at 940 and 610 cm^{-1}, respectively. The range of 1000–500 cm^{-1} has an increased overall intensity caused by the extra broad band of water librations. This mostly affects ATR and PAS measurements.

3.2 Signal-gathering depth and PAS modulation frequency comparison

The refractive index of nanodiamonds is not equal to the refractive index of diamond due to the developed surface and the presence of many surface groups [16], but it is likely that the refractive index of nanodiamonds of any grade is within the value 2.4 ± 0.1 [50]. Thus, the estimation of the penetration (signal-gathering) depth by ATR, Eq. (1) at 4000 cm^{-1} gives the value is 240 nm, which is comparable to the characteristic size of ND clusters [44, 51, 52]. The maximum penetration depth of radiation in ATR measurements for a wavenumber of 400 cm^{-1} is *ca.* 2.4 μm, which is more than two orders of magnitude larger than the particle size of the studied nanodiamonds. This correlates with a very low sensitivity and reproducibility of measurements of ATR of ND surface groups approximately up to 2000 cm^{-1}.

To estimate the penetration depth of radiation by PAS-FTIR, we performed a model calculation of μ_s for interferometer modulation frequencies (IMF) of 1.6, 2.5, and 10 kHz using Eq. (2), Fig. S1 (Appendix A). The penetration depth of radiation in all the mid-IR range is 300–1000 μm, which is much greater than the size of the investigated particles (0.1–0.2 μm). Therefore, the radiation must pass completely through all particles and each individual particle emit thermal waves in all directions of space and give a high signal to the detector [53].

The PAS-FTIR spectrum of nanodiamonds at 2.5 kHz has a large baseline profile in the range of 4000–1900 cm^{-1}. The absorption bands of stretching $–CH_x$ vibrations of asymmetric (2920 cm^{-1} and symmetric 2860 cm^{-1} [43, 54] remain in the spectra. The reason for the differences in spectra is the selection of the amplification mode for the sample signal. A twofold change in the signal amplification mode and a slight decrease in the radiation penetration depth causes significant changes in the spectrum. In both spectra, the band of stretching vibrations –C=O at 1750 cm^{-1} [45], and the band of stretching vibrations of the deprotonated carboxyl group at 1680 cm^{-1} [45] are manifested. There is also a band of asymmetric stretching vibrations of deprotonated carboxyl –C=O 1550 cm^{-1} [44, 45]. Anyway, at 1.6 kHz, the band of asymmetric stretching vibrations of the carboxyl C–O stretch at 1270–1250 cm^{-1} and symmetric C–C–C vibrations with a wavenumber of 1190–1100 cm^{-1} [36, 44, 49] are weaker. The 970 cm^{-1} band of C–O–C bending vibrations [54] has a high intensity. PAS-FTIR spectra at an IMF of 5 kHz shows the same bands as lower IMF with the signal-noise ratio, thus with degraded information. A serious difference between low and high IMFs may result from thermal scattering that increases the overall background in PAS. Thus, high IMFs for PAS of nanodiamond powders are not recommended.

3.3 Band reproducibility

For ATR–FTIR and DRIFT, the shape of the all the test bands and the positions of the maxima are reproduced, except for the 1750 cm^{-1} band (carboxyl C=O), where a small scatter is observed after vector normalization. The range of 3000–2000 cm^{-1}, in addition to absorption bands of CH_x stretching vibrations contains CO_2 absorption bands and, in ATR, the absorption band of the ATR attachment crystal (2350–1900 cm^{-1}), which seriously degrade the reproducibility of ATR measurements in this range. In the range of 2000–1000 cm^{-1}, the band at 1400 cm^{-1} (C–O/C–H) has the highest RSD value among all the analyzed bands due to its lowest intensity in this range. In the range of 1000–400 cm^{-1}, a significant increase in the baseline is observed due to water librations, which entails the need for a baseline-correction procedure.

Preprints (www.preprints.org) | NOT PEER-REVIEWED | Posted: 30 November 2020 doi:10.20944/preprints202011.0740.v1

For PAS-FTIR (IMF, 1.6 kHz), the shapes and positions of band maxima are also reproduced. In the range of 4000–3000 cm^{-1}, many narrow bands in the range 3920–3550 cm^{-1} observed, which belong to stretching vibrations of adsorbed water either on the walls of the IR spectrometer and attachment or on the surface of nanodiamonds. After the vector normalization procedure, main absorption bands at 1760 and 1630 cm^{-1}, as well as 1267 cm^{-1} are most clearly traced. High-intensity artifacts are observed in the range 500–400 cm^{-1}, which is why this range is not considered further in PAS. For two spectra out of ten, artifacts are observed in the entire range over the entire considered range of wavenumbers. The bands at 1400 and 1750 cm^{-1} have the best RSD values. As we showed in the previous section, the particle size of nanodiamonds is significantly lower than μ_{ATR} in the whole spectral range. However, decreasing the radiation penetration depth upon shifting from the IMF from 1.6 to 2.5 kHz lowers the intensities of all the characteristic bands and increases RSD values, thus negatively affecting the signal-to-noise ratio. Thus, to record a PAS-FTIR spectrum of nanodiamonds in the range 4000–2000 cm^{-1}, it is preferable to use an IMF of 1.6 kHz with a 200-fold amplification of the background signal and a 1000-fold gain of the sample signal.

The measurement errors for mid-IR spectra can be summed up as follows (spectra reproducibility errors were found by Eq. (3); spectra at this stage were not subjected to automatic baseline correction and smoothing). The RSD values of the integrals of the main bands (Table 5) are presented in Tables 6 and 7 for ATR and PAS-FTIR, respectively. In the range 4000–3800 cm^{-1}, the error can be up to 100% in PAS-FTIR; in ATR-IR and DRIFT, the error does not exceed 35%. In 3800–3000 cm^{-1}, the error is 15–30% for all the techniques. In 3000–2500 cm^{-1}, the error for PAS-FTIR is also 15–30%; for ATR is lower, 18–20% (in the absorption range of the diamond crystal, 2350–1900 cm^{-1}, 35–45%); for DRIFT is 10–15%. In 1900–1000 cm^{-1}, the minimum error in PAS-FTIR is 25%, and no more than 15–25% for ATR, and 12–20% for DRIFT. In 1000–400 cm^{-1}, the error for PAS-FTIR and DRIFT does not exceed 40%; in ATR, does not exceed 20%. Therefore, for NDs, DRIFT shows the best results; the second best is ATR despite the possibility of mechanical damage to the diamond crystal of the ATR attachment. The spectra are well reproduced, the baseline is less distorted and stable apart from the 1000–400 cm^{-1} range, and no spectral artifacts appear in the whole interval. The same cannot be said about the PAS-FTIR spectra, showing some spectral artefacts. However, in general, RSD profiles are similar; most differences are observed in the absorption range of the diamond crystal of ATR attachment (2350–1900 cm^{-1}).

Table 6. Relative standard deviation band integral intensities in the wavenumber range 3000–2000 cm^{-1} by ATR-FTIR (RDDM ND brand)

Band center, cm^{-1}	High-wave boundary, cm^{-1}	Low-wave boundary, cm^{-1}	RSD
2935	2952	2918	0.98
2837	2857	2817	1.41
2650	2673	2626	0.14
1750	1815	1684	0.18
1630	1668	1535	0.18
1400	1417	1393	0.24
1270	1341	1249	0.20

Table 7. Relative standard deviation band integral intensities in the wavenumber range 3000–2000 cm^{-1} by PAS-FTIR (RDDM ND brand)

Band center, cm^{-1}	High-wave boundary, cm^{-1}	Low-wave boundary, cm^{-1}	RSD
1750	1852	1691	0.15
1630	1690	1594	0.29
1460	1482	1442	0.39
1400	1441	1353	0.09

Preprints (www.preprints.org) | NOT PEER-REVIEWED | Posted: 30 November 2020 doi:10.20944/preprints202011.0740.v1

4. Discussion

4.1 DRIFT

This modality provides the maximum number of bands and shows the highest sensitivity in the whole range, from NIR to FIR. The bands discussed above for the NIR range above 4000 cm^{-1} are obtained only with this modality due to a lower noise in DRIFT.

In this paper, we used DRIFT with a bare mirror as the background reference sample, the technique that is used for detector or spectrometer calibration [55] but more seldom used in practical DRIFT analysis. The used DRIFT attachment also allows diffuse-reflectance measurements without sample dilution with KBr, without a change in the reproducibility and sensitivity (Fig. 11).

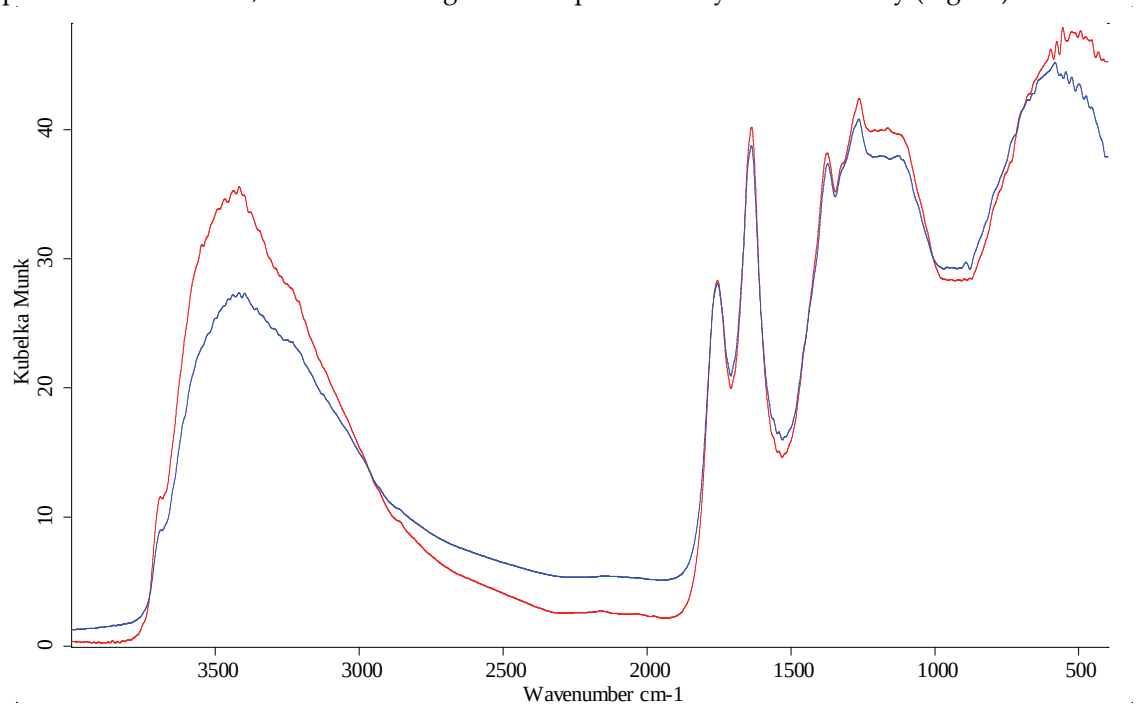

Figure 11. Diffuse reflectance mode, DLaTGS detector, RUDDM nanodiamonds, red – Praying Mantis mirror was used for background collection, blue – KBr at sample cup was used for background collection. Spectra were smoothed (13 points) and normalized to maximize each spectrum.

This modality is capable of hydrogen-bond continua at 3900–3000 cm^{-1} and 2700–2500 cm^{-1}. The latter range can be seen only with DRIFT, as ATR has not enough sensitivity, while PAS shows a high-level noise. As shown in Section 3.3, this range suffers an increase in the noise level due to diamond crystal absorption. The range 2400–2300 always shows the artefact peaks of gaseous CO_2.

DRIFT also provides the best resolution and sensitivity towards hydrocarbon constituents of ND shell: CH_x groups at 3000–2700 cm^{-1}. These are accompanied with CH_2/CH_3 deformation bends at 1400 and 1370 cm^{-1}, respectively (usually as shoulder bands); however, these bands could also have the oxygen-containing components. Also, this modality provides well resolved and intense bands at, 1450 cm^{-1} (C–O–H bend and $–CH_2$ wag vibrations); thus, these ranges would require either a sample preparation or another modality.

Depending on the brand, the CH_x range in DRIFT shows stretch aromatic vibrations at 3100 cm^{-1} with rather high sensitivity and correlated bands 940 ($=CH_2$ wag) and 830 cm^{-1} (aromatic –C–H bend), Figs. 1, C, 3, C and 4B, 5B, and 6B. Some brands show a weak band at 760 cm^{-1} (Figs. 1,C and 4,B) that can be attributed to polyaromatic bend vibrations, and the latter band is not seen neither in

Preprints (www.preprints.org) | NOT PEER-REVIEWED | Posted: 30 November 2020 doi:10.20944/preprints202011.0740.v1

PAS, nor in ATR modalities. Carbon-carbon bonds are represented by 1560 cm^{-1} (alkene/aromatic stretch) and 410 cm^{-1} (in-phase vibrations).

Carbonyl band at 1760 cm^{-1} is most intense in the range 1900–1300 cm^{-1} (Figs. 1B, 2B, and 3B). The right shoulder band at 1790 cm^{-1} (conjugated carbonyl groups) is less pronounced compared to ATR and PAS (DNA-TAN and DNA-STP brands).

The H–O–H band at 1610 cm^{-1}, which we assign more tightly bound water is weaker than in PAS and especially ATR. This allows revealing actual bands belonging to asymmetric C=O and C=C stretches in this area (PL-D-G01P, UDA-S, UDA-SP, and DNA-STP).

Despite most intense bands in the range of 1400–1200 cm^{-1}, it is not well-resolved (Figs. 1C, 2C, and 3C) most probably due to saturation effects [56], and this range is not expedient for band comparison.

Of special interest in DRIFT modality is the range 2300–2000 cm^{-1} that is not informative in ATR with a diamond crystal due to diamond adsorption and PAS due to a high noise level. This range shows a series of rather broad and rather weak bands located at 2230, 2140, and 2050 cm^{-1} (Figs. 1B, 2B, and 3B, insets). The appearance and relative intensity of these bands depends on the ND brand. These bands could be surface groups bound to metal species or nitrile [57] or other C–N–C, C–N–N and similar nitrogen-based vibrations [58], which may be the manifestation of N or N vacancy centers in the ND cores [59]. These bands were found in graphene [12] but require more studies in the case of nanodiamonds. The complete elucidation of these groups is more difficult compared to other groups as only DRIFT modality can be used. The comparison of detectors shows that the selection does not significantly affect the band quality in this range, although photovoltaic detection tends to produce unresolved bands.

From the viewpoint of different aggregates in ND samples or different characteristic sized in ND brands, DRIFT measurements should be corrected to radiation reflections from particles of different sizes [56], and a direct comparison with DRIFT may not be very correct, and require a special attention.

4.2 ATR-FTIR

Due to low sensitivity in the far and Mid-IR range in 4000–2000 cm^{-1}, ATR spectrum shows little-to-no information in this range, CH_x bands are only seen for several brands (UDA-GO-SP family). As well, in the range the band of stretching vibrations of –O–H linked by hydrogen bonds, 3690 cm^{-1}, is observed only in some brands and a weaker band at 3715 cm^{-1} is not seen with a DLaTGs detector, and is very weak with a photovoltaic detector (Fig. 12). Some spectra show a low-intensity sharp artefact band at 2660–2650 cm^{-1} over-imposed with the weak and broad carboxylic O–H stretch visible in some brands only.

Preprints (www.preprints.org) | NOT PEER-REVIEWED | Posted: 30 November 2020 doi:10.20944/preprints202011.0740.v1

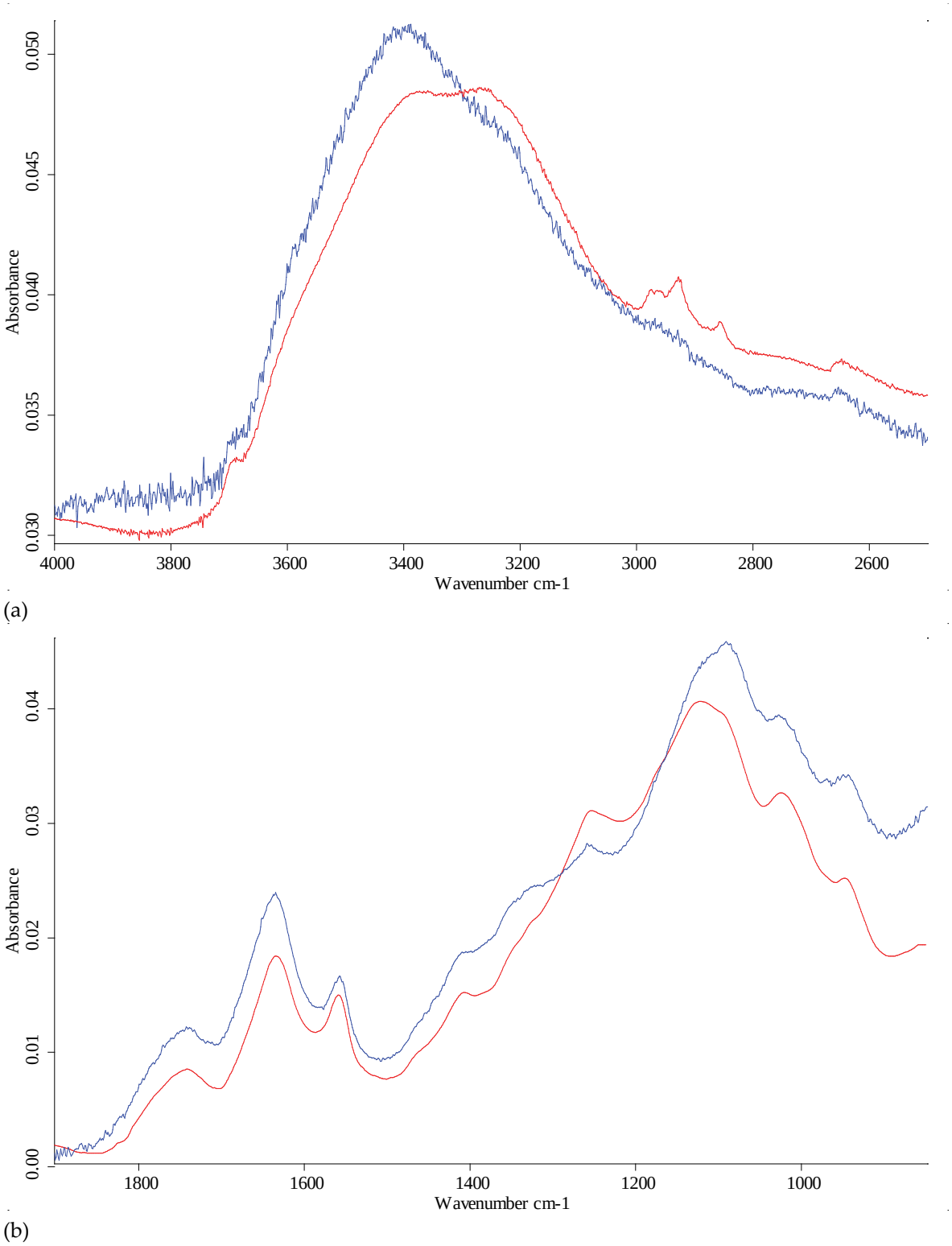

Figure 12. ATR mode, UDA-SP nanodiamonds, red – LN-MCT photovoltaic detector, blue – DLaTGS detector **(a)** 4000–2500 cm^{-1}, **(b)** 2000–800 cm^{-1} range. Spectra were not smoothed but normalized to maximize each spectrum.

Among oxygen-containing groups, the carbonyl C=O stretch (1770–1760 cm^{-1}) bands in ATR spectra is the strongest. Compared to DRIFT, ATR band at 1760 cm^{-1} shows a shoulder band at 1790–1800 cm^{-1}, which can be attributed to anhydride or similarly strongly bound carbonyls. This band is weaker than the neighboring band of water band at 1630 cm^{-1} and at 1270 cm^{-1} correspond to

Preprints (www.preprints.org) | NOT PEER-REVIEWED | Posted: 30 November 2020 doi:10.20944/preprints202011.0740.v1

carboxyl C–O stretch, and at 1100 cm^{-1} to non-carboxyl C–O stretch. In general, the band at 1770–1760 cm^{-1} is visible, but its intensity is lower than in DRIFT and PAS modalities.

Other characteristic bands in ATR spectra are H–O–H bending vibrations (loosely bound, 1643 cm^{-1} and strongly bound, 1620–1635 cm^{-1}). All other bands attributed to water in the low-wave Mid-IR range are well pronounced as well. The problem of water-vapor artefact bands at 1580–1500 cm^{-1} is least pronounced in ATR due to the minimum effect of water vapors due to low signal-generating depth; however, the intensity is lower compared to other modalities, and, if ATR modality is selected, a high-sensitive detector is required.

Also bands of 1485 cm^{-1} (–CH_2 wag), at 1390–1370 cm^{-1} (–CH_2 deformation and C–O–H in-plane bend) are also visible, while the weak band at 1440 cm^{-1}, which is attributed to aromatic ring stretch/C–O–H does not appear. It is noteworthy that many of these bands can be attributed to the different types of functional groups (hydrocarbon and oxygen-containing) and their intensities are much lower than in the case of DRIFT. Along with lower intensity of carbonyl bands compared to DRIFT, this may evidence that ATR is more sensitive to the hydrocarbon layers than functional groups. This range is, thus, quite important to be probed with two IR modalities as the ratios.

ATR becomes the dominant modality for 1100 cm^{-1} and below, when DRIFT shows more enveloping bands and PAS shows the saturation effects and high noise levels. The ATR-FTIR spectrum has a weakly pronounced band at 940 cm^{-1} (Figs. 4B, 5B, and 6B), which is not revealed in DRIFT and PAS. To the contrary, these two modalities show a band at 960 cm^{-1}, but the intensity of 940 cm^{-1} is quite low. In our opinion, this band at 960 cm^{-1} is non-carboxyl out-of-plane C–O–H bend, while the peak at 940 cm^{-1} is =CH2 wag that is revealed in brands with a large contents of nonsaturated/aromatic hydrocarbons (UDA-SP, D-G01P brands). The same situation is for the band at 830 cm–1 (aromatic CH_2). A characteristic band at 410 cm^{-1} is clearly visible only in ATR and can be attributed to C–C in-phase vibrations [41]. However, the bands at 760 and 610 cm^{-1} have lower intensities compared to other modalities.

4.3 PAS-FTIR

In general, PAS-FTIR spectra at IMF of 1.6 and 2.5 kHz are similar to DRIFT and show the same intensity ratios. For most brands spectra at IMF of 1.6 and 2.5 kHz are the same relative to intensity ratios. In the range 4000–3600 cm^{-1}, PAS exhibit weak stretching vibration bands of isolated hydrogen bonded species at 3780 cm^{-1} [36], which is not visible with other modalities, and the sensitivity towards other hydrogen-bonded species is similar to DRIFT. Bands at 1750, 1640, 1250, and 1100 cm^{-1} are present in all FTIR-PAS spectra for the whole IMF range 1.6–10 kHz.

Weak bands of asymmetric CH_x vibrations in the range 2955–2920 cm^{-1} are pronounced, and the sensitivity is the same as in the case of DRIFT, while the sensitivity towards symmetric vibrations seems lower than in DRIFT. The range 2700–1900 cm^{-1} is noisy, contains the CO_2 peaks and not informative.

As in ATR, the carbonyl band at 1760 cm^{-1} shows a shoulder at 1790 cm^{-1} of conjugated carboxyls. The bands at 1610 and 1560 cm^{-1} characteristic to some bands are quite intense as in DRIFT; and in this range, PAS provides the same resolution (Fig. 7A, B, and C). However, in this range PAS experience the maximum effect from water vapor peaks, so this can lead to a wrong interpretation of the results (because of negative water vapor sharp bands). Thus, DRIFT seems the most expedient in this range. However, the CH_2 band at 1450 cm^{-1} is almost hidden being in the shoulder of the more intense C–O–H broad band at 1330 cm^{-1}.

In a PAS-FTIR spectrum recorded with an interferometer frequency of 2.5 kHz or higher, PAS-FTIR provides a different picture in 1900–1500 cm^{-1} range compared to DRIFT and ATR. PAS FTIR shows a different ratio of intensities of major bands of C=O stretch of isolated carboxyl group at 1760 and band of HOH vibrations (1635–1620 cm^{-1}). While in almost all the brands, the C=O band has the maximum intensity compared to other bands, in PAS this band is higher in intensity only for an IMF 1.6 kHz, while for IMFs of 2.5–10 kHz, the most intense is the water band.

For the range 1500–1000 cm^{-1}, the band at 1100 cm^{-1} (non-carboxyl C–O stretch) is equally strong as in DRIFT and ATR-FTIR, but PAS-FTIR shows higher sensitivity to bands at 1330 and 1260

Preprints (www.preprints.org) | NOT PEER-REVIEWED | Posted: 30 November 2020 doi:10.20944/preprints202011.0740.v1

cm^{-1} compared to DRIFT and the shape of IR spectra in this range is coincident with ATR spectra. The range 1400–1200 cm^{-1} is less resolved compared to ATR but still have higher sensitivity compared to ATR. The region of 1200–900 cm^{-1} is not well-defined intensity-wise, as the intensities are distorted due to saturation effects [33, 60], which was previously shown to have effect on PAS identification for soil nanoparticles [31].

Comparison with DRIFT shows almost the same situation as FTIR-PAS to ATR comparison: matrix vibrations mode intensities in DRIFT are degraded, although seen clearly; and in concordance with literature, much lower sensitivity in 2500–2000 cm^{-1} region is shown compared to FTIR-PAS [61].

Contrary to DRIFT, especially under the conditions of rapid-scan modes used in this study, FTIR-PAS spectra are mainly affected with thermal penetration depth, which is governed by thermal parameters of ND diamond matrix and independent from the particle size. Thus, FTIR-PAS spectra become directly comparable from the viewpoint of composition more readily, while retaining most features of DRIFT unrevealed in ATR spectra. In the frames of this study, no significant differences between PAS and DRIFT spectra were observed (Fig. 7).

4.4 ND Brand features

The aim of this study was not the complete characterization of specific brands, but differences in the composition are obvious can be used as examples of capabilities of different IR modalities in ND analysis.

All the brands differ in the position of the main maximum and the width of the band of carbonyl at 1750 cm^{-1}. For most brands it is located at 1740 cm^{-1}, for DNA-TAN and DNA-STP it is located at 1786 cm^{-1}, for RUDDM, 1760 cm^{-1}, and for PL-D-G-01 and PL-D-G02 it is pure bimodal with 1780 and 1750 cm^{-1} maxima (Figs 1B and 4C). The reproducibility of this band is highest among the other bands in the spectrum and it is usually the same for different brands of the same manufacturer (DNA-TAN and DNA-STP). For most ND brands, this band is a rather wide continuum with a width of 300 cm^{-1} overlapped with the water peak at 1640 cm^{-1}, but its left shoulder is well resolved (Figs. 1B, 2B, 3B, 4C, 5C, 6C). The shape of this band is not affected by drying (Figs. 9 and 10).

From the viewpoint of ND brand characterization, these groups of nanodiamonds can be distinguished by the amount of bound water (1630 cm^{-1}) and the intensity of OH continuum 3600–3000 cm^{-1} and carboxyl C=O and C–O–H bands at 1760–1740 and 1440–1340 cm^{-1}. Upon drying, the spectra of such brands show a decrease in the bands associated with loosely bound water, while the intensities of carboxyl bands remain the same. For RUDDM brand, Figure 3A shows that a decrease in the peak at 3695 cm^{-1} (water hydrogen bonds, there is an increase in the band 3715 cm^{-1} (hydrogen bonds for non-water species). Also, these brands do not show a separate band of loosely bound water at 1643 cm^{-1}, it is revealed as a blue-shifter asymmetry of the 1630 cm^{-1}band.

It is noteworthy that the intensities and intensity ratio 1760/1630 cm^{-1} and other peaks in the range 1900–1500 cm^{-1} can probably be used for ND brand selection. The nanodiamonds with high colloidal solubility have higher intensities of both major bands, and usually sharper shapes, which may evidence a domination of single moieties at the surface (carboxyl groups) and larger amounts of bound water. Also the peak at 1760 cm^{-1} is located at 1760–1750 cm^{-1}, which corresponds to the existing data on carboxyl carbonyl and is accompanied with bands at 1460–1440 cm^{-1} (carboxyl C–O–H) and larger intensities of –O–H continuum at 2650 cm^{-1}. The intensity of carboxyl band is higher than in water band. 'Insoluble' NDs have a water peak which is more intense than carboxyl band and it is accompanied with more tightly bound water peaks at 1610–1550 cm^{-1}; other carboxyl-related bands have lower intensities and other C–O bands are more intense.

Thus, these two bands can be used for the preliminary estimation of their properties in aqueous solutions, and for monitoring the properties upon thermal or directed chemical treatments. Our studies show that any FTIR modality can be used for this, with ATR having the advantage of working with small amounts and dried dispersions, while DRIFT provides better sensitivity, better distinguishing of signal from gaseous water artefact peaks. In this task, PAS does not have real

Preprints (www.preprints.org) | NOT PEER-REVIEWED | Posted: 30 November 2020 doi:10.20944/preprints202011.0740.v1

advantages from the viewpoint of sensitivity and resolution, if other bands in spectra are not considered.

From the viewpoints of classification, C–H bands provides relevant information with rather different composition of brands. Most brands, aliphatic CH_2 (2940–2930 and 2850 cm^{-1}) have the maximum intensity of corresponding bands evidencing the contribution from long aliphatic chains. In several cases, like RDDM, this correlates with the graphite as the ND production source. However, UDA-GO-SP-M1 and UDA-GO-SP-M2 show the predominant peaks at 2950 and 2880 cm^{-1} corresponding to CH_3 groups and PL-D-G01P reveals similar intensities of CH_2 and CH_3 bands. UDA-GO-SP-M1 and -M2 also show a medium-intensity bands at 2970 cm^{-1} of alkene groups. Several brands, PL-D G01P and RUDDM also show a high intensity of bands over 3000 cm^{-1} assigned to aromatic compounds which, in the latter case, correlates with the manufacturers' information of the ND source material, trinitrotoluene. This correlates with the bands at 1000–700 cm^{-1} (Table 5) attributed to aromatic C–H vibrations. Brands with high contribution from C–H have distinct bands in near IR DRIFT 4800–4100 cm^{-1} (Figs. 1A, 2A, and 3A). To sum up, a detailed study of C–H composition of NDs may require both DRIFT and ATR modalities to have the maximum sensitivity in high-frequency and low-frequency part of spectra to provide a cross checking in different spectral ranges and modalities. However, some caution in this is in order: such bulk spectra relate to nanodiamonds as materials, which in fact can contain ND clusters as well some accompanying components that may seriously affect IR spectra. For instance, ND analysis of visible spectra of some ND brands with visible transmission/optoacoustic spectroscopy with multistage centrifugation reveals a smallest non-diamond sp^2 fraction [52], which can affect the overall unfractionated sample spectra.

Apart from major bands than can be used for general estimations of ND brands, spectra in different modalities and detectors reveal a more detailed difference in NDs. For instance, PL-D G01P, UDA-S and UDA-SP, and DNA-STP form a specific subset of ND brands of different manufacturers, which have several common features, already discussed above upon modality comparison. They have distinct bands at 1610 and 1560 cm^{-1} that are absent in most other brands (Fig. 8). The band at 1560 cm^{-1} is considered the most uncertain for complex samples [30] and can be attributed to carbon bonds [62-64] and absorbed water. It is noteworthy that the brands with the distinct band at 1560 cm^{-1} have the main water band red-shifted compared to the most common position of 1635 cm^{-1}. For UDA-GO-SP and PL-D G01P, the ATR spectrum contains only one band of stretching vibrations of the carbonyl group –C=O at 1750 cm^{-1} like other brands while in DRIFT and PAS-FTIR a low-intensity band of deprotonated carboxyl at 1680 cm^{-1} appears [45], which distinguishes this brand from other counterparts even of the same manufacturer. It is noteworthy that PL-D G01P shows a structure of the band of 1630 cm^{-1} with maxima at 1646, 1636, and 1626 cm^{-1} and a band at 980 cm^{-1} (Fig. 8). The brands with the high intensity of CH_x bands (UDA-GO-SP-M1 and UDA-GO-SP-M2 and PL-D G02) show a intensity band at 1190 cm^{-1} that can be assigned to C–C(O)–C vibrations.

From the viewpoint of C–H features, many brands also reveal some specific features. UDA-GO-SP-M1 and UDA-GO-SP-M2 are very similar and apart from highest intensity of CH_3 bands among all the studied NDs (Fig. 3 and 6) and a shoulder band at 1670 cm^{-1} appears (DRIFT), which can be attributed to C=C stretch (Table 5). As well, UDA-GO-SP-M1 and UDA-GO-SP-M2 brands shows a distinct band at 830 cm^{-1} (Fig. 6C). PL-D-G01 is distinguishable from all other brands by a series of sharp and rather intense bands at 920, 880, 830, 800, 785, 770, and 740 cm^{-1} (Fig. 13) that can also be attributable to aromatic chains, as well as the high intensity of the band at 630 cm^{-1}. PL-D-G01P shows intense bands at 1480 cm^{-1} (C–C aromatic stretch, Fig. 1, C) and 3035 cm^{-1} (C–H aromatic stretch, Fig. 1, B).

Preprints (www.preprints.org) | NOT PEER-REVIEWED | Posted: 30 November 2020 doi:10.20944/preprints202011.0740.v1

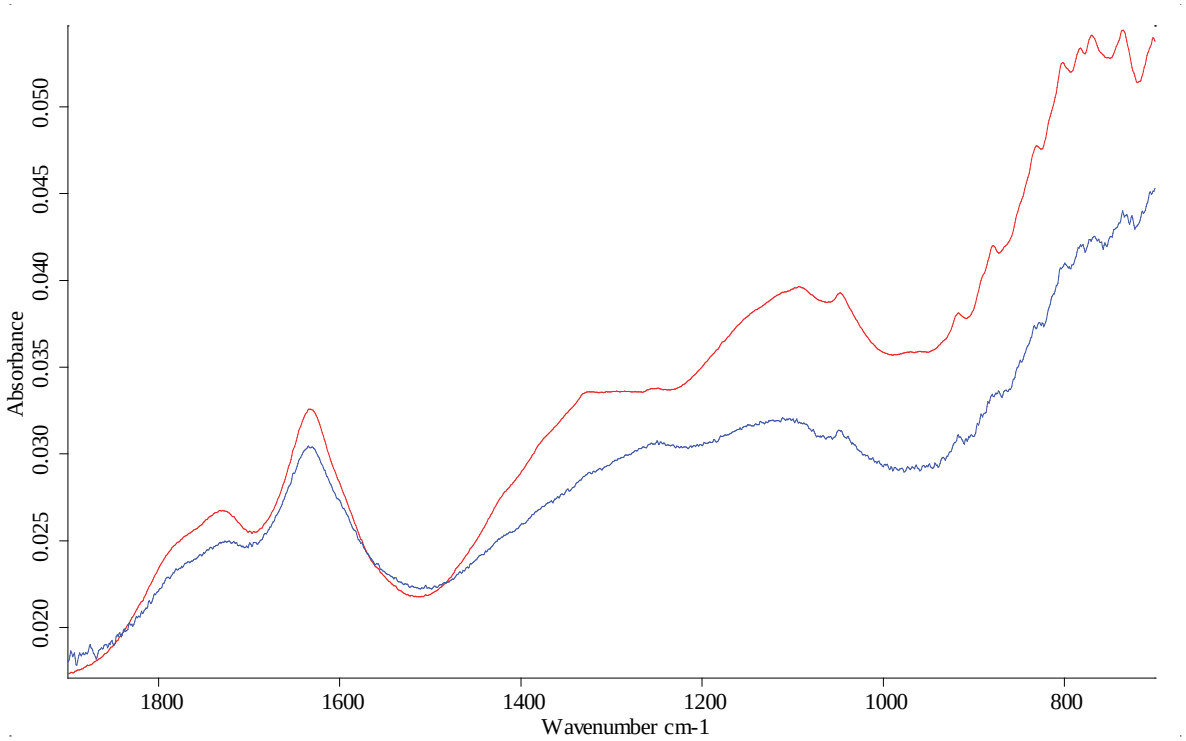

Figure 13. ATR mode, PL-Nanopure-G01P nanodiamonds, red – LN-MCT photovoltaic detector, blue – DLaTGS detector. Spectra weren't smoothed but normalized to maximize each spectrum.

As we mentioned in the previous sections, the range 2300–2000 cm^{-1} is characterized with a series of weak rather sharp bands, which are very characteristic for certain brands. The band at 2230 cm^{-1} is characteristic to UDA-GO-SP, PL-D-G01 P, UDA-TAN, PL-D G01, and the band at 2050 cm^{-1} is present in DRIFT spectra of different brands (Figs. 1B, 2B, and 3B, insets), UDA-GO-SP-M1, UDA-GO-SP-M2, UDA-SP, SDND, and RUDDM. In several cases, this band falls within the left shoulder of the continuum band of the carbonyl, so it is completely undetectable. The band at 2140 cm^{-1} is characteristic for most brands and is the only band in this range for UDA-S, UDA-S-GO, and PL-D-G02.

4.5 Modality Comparison

Contrary to some similar studies on IR modality comparison for complex objects [30, 31, 37, 65, 66], we cannot conclude that all the modalities are equal in ND characterization and can be used alone. Though it is rather obvious that all the modalities can provide the relevant information on ND surface composition, not a single modality provides the whole information, and the combination of modalities seems quite important. In our opinion, it could result from the DRIFT conditions used in this study: to the contrary of other studies [30, 31, 37, 65, 66], we used a bare mirror as a reference sample, which decreased the noise and provided the good sensitivity and reproducibility. Also, using an attachment that provided diffuse-reflection measurements with sample dilution and change provided much more valuable information from DRIFT spectra and made this technique most informative and reliable for ND characterization.

Although in several cases, ATR has the advantage of small sample amount, still DRIFT seems to be the best choice as it provides the good sensitivity (especially with a photovoltaic detector, Fig. 14) and the widest spectral range of near IR and Mid-IR that contains the most important information on NDs. The best sensitivity of DRIFT in hydrogen-bond, CH_x, and C=O/water ranges makes it possible to distinguish various trademarks, monitor the changes during the surface modification and thermal treatment and other studies. The range of 1200–400 cm^{-1} has the secondary value in DRIFT due to saturation and lower sensitivity. High sensitivity of DRIFT provides a rather detailed study in CH_x

Preprints (www.preprints.org) | NOT PEER-REVIEWED | Posted: 30 November 2020 doi:10.20944/preprints202011.0740.v1

range and the low-intensity peaks in 2700–2000 cm^{-1} range that cannot be revealed by other modalities. Still, cross-examination of ND brands with DRIFT may be taken with caution due to the particle-size effect. From the viewpoint of C–H characterization of ND surface, DRIFT modality has the obvious advantage of sensitivity in the whole mid-IR range, while ATR provides a more unified picture distinguishing high CH_x/low CH_x brands only; however it provides the additional information due to high sensitivity in the far IR region, e.g. the C–C peaks at 410 cm^{-1}.

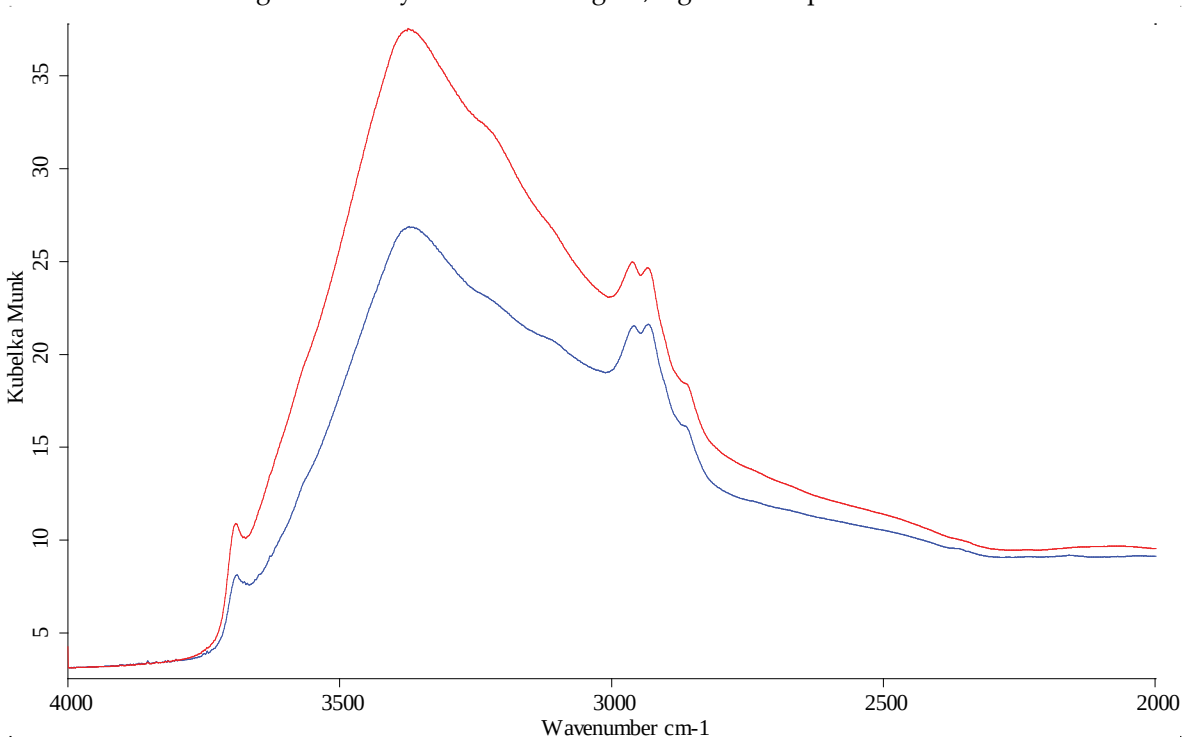

(a)

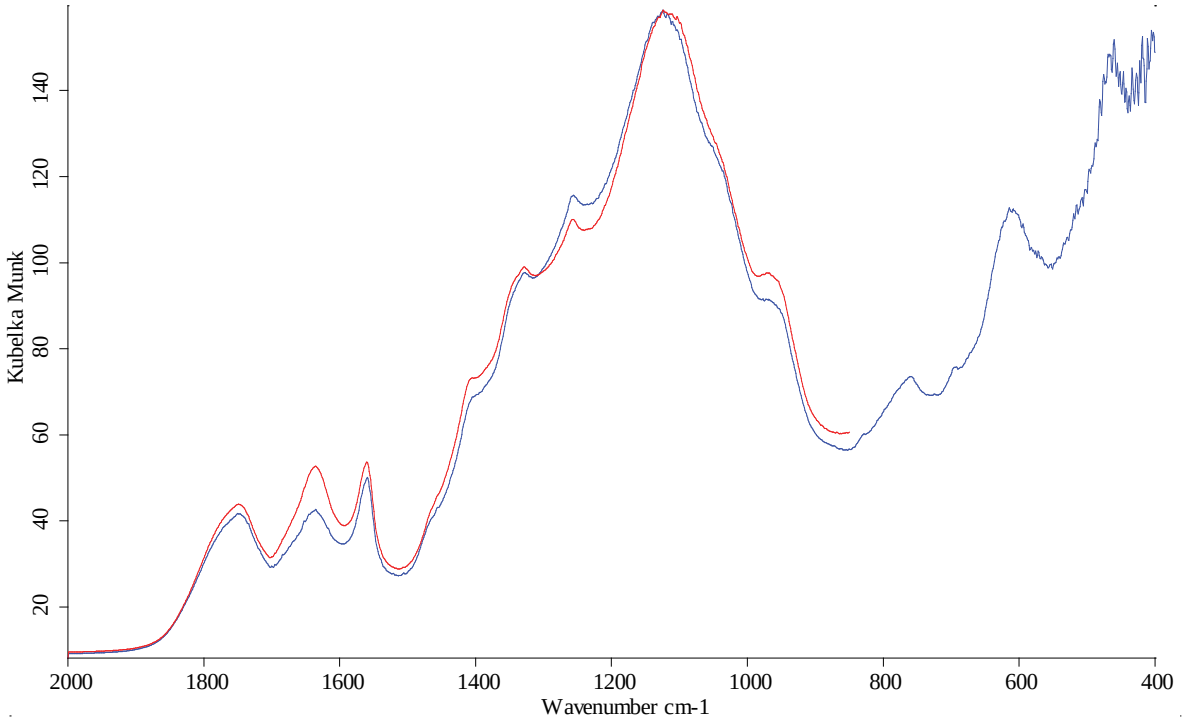

(b)

Figure 14. Diffuse reflectance mode (mirror was used for background collection), UDA-SP nanodiamonds, red – LN-MCT photovoltaic detector, blue – DLaTGS detector **(a)** 4000–2000 cm^{-1}, **(b)** 2000–400 cm^{-1} range. Spectra were not smoothed but normalized to maximize each spectrum.

Preprints (www.preprints.org) | NOT PEER-REVIEWED | Posted: 30 November 2020 doi:10.20944/preprints202011.0740.v1

ATR provides the good sensitivity for liquid-water and C–H bands in nanodiamond spectra in the range 2000–400 cm^{-1} but shows mediocre sensitivity towards the medium and minor bands that are attributed to carbon-oxygen bands. This makes this modality most expedient for monitoring the drying and surface oxidation of nanodiamonds as these processes change the major functional groups and water [5], while retaining the reference points of C–H bands. The ND brand comparison, which is based on CH_x bands at 3000 cm^{-1} and minor oxygen-containing groups using ATR is probably less expedient, and DRIFT or PAS should be used instead. ATR can be used as a secondary, checking technique with DRIFT due to its higher sensitivity in 2000–400 cm^{-1} range, lower effects from gaseous water, and better resolution in the ranges (Fig. 15), when DRIFT and PAS techniques experience optical or thermal saturation. In ATR spectra, the spectral information in the range of 2700–1900 cm^{-1} is lost due to absorption of the diamond crystal itself and closeness of nanodiamond/diamond refractive index. Also, in 1100–400 cm^{-1} water librations should be taken into account. Also, our experiments show that detector sensitivity is quite important in ATR, and a room-temperature DLaTGs detector can be recommended for major band monitoring, while a photovoltaic detector serious increases the spectral information (Fig. 16), making ATR closer to PAS, while retaining all the advantages of ATR.

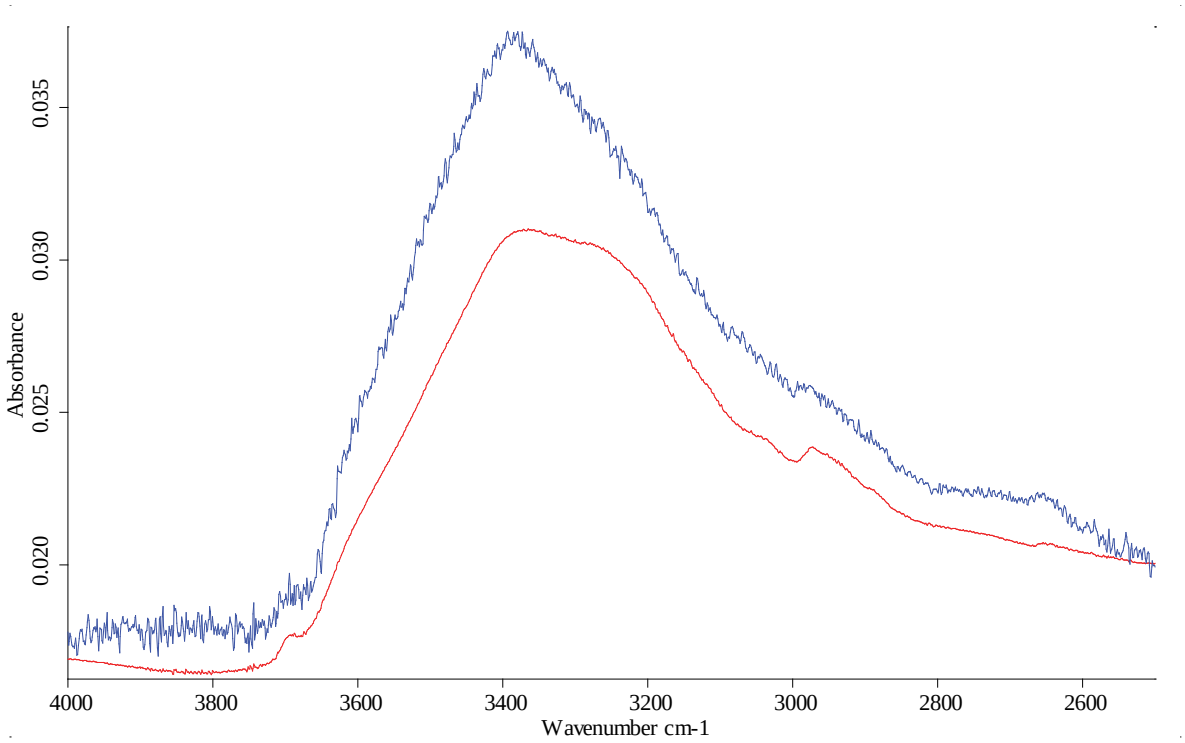

(a)

Preprints (www.preprints.org) | NOT PEER-REVIEWED | Posted: 30 November 2020 doi:10.20944/preprints202011.0740.v1

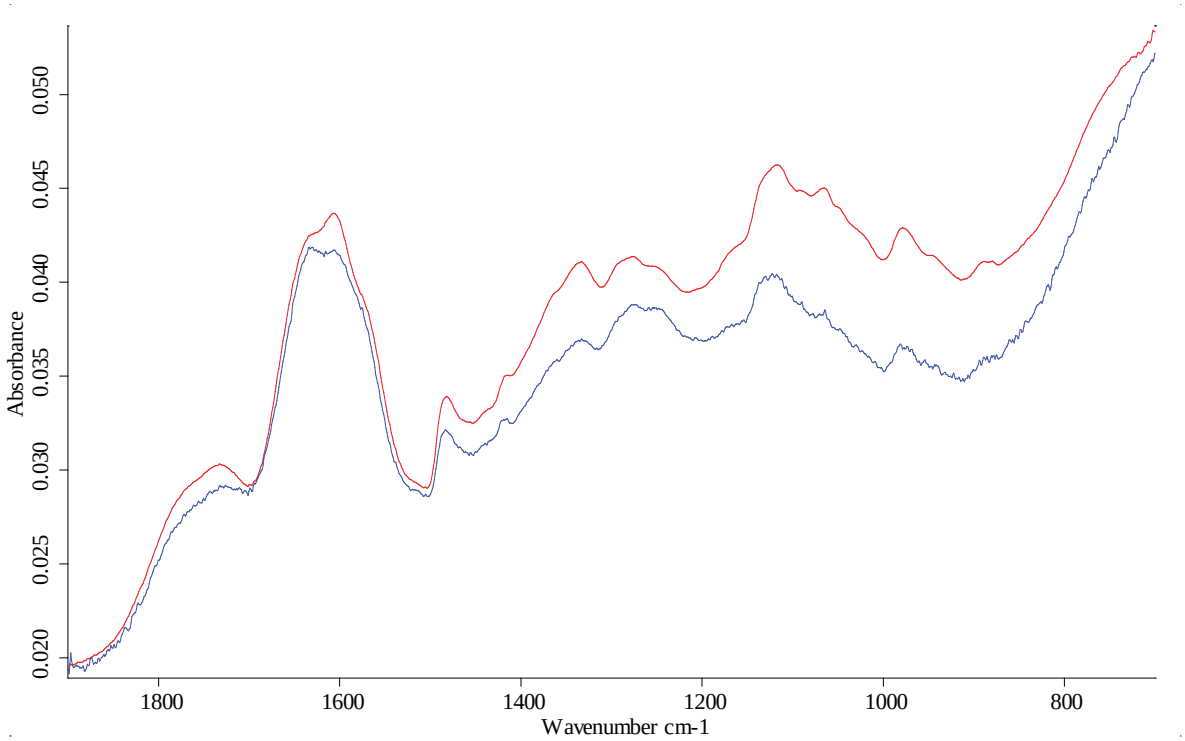

(b)

Figure 15. ATR mode, PL-D-G-01P nanodiamonds, red – LN-MCT photovoltaic detector, blue – DLaTGS detector **(a)** 4000–2500 cm^{-1}, **(b)** 2000–800 cm^{-1} range. Spectra were not smoothed but normalized to maximize each spectrum.

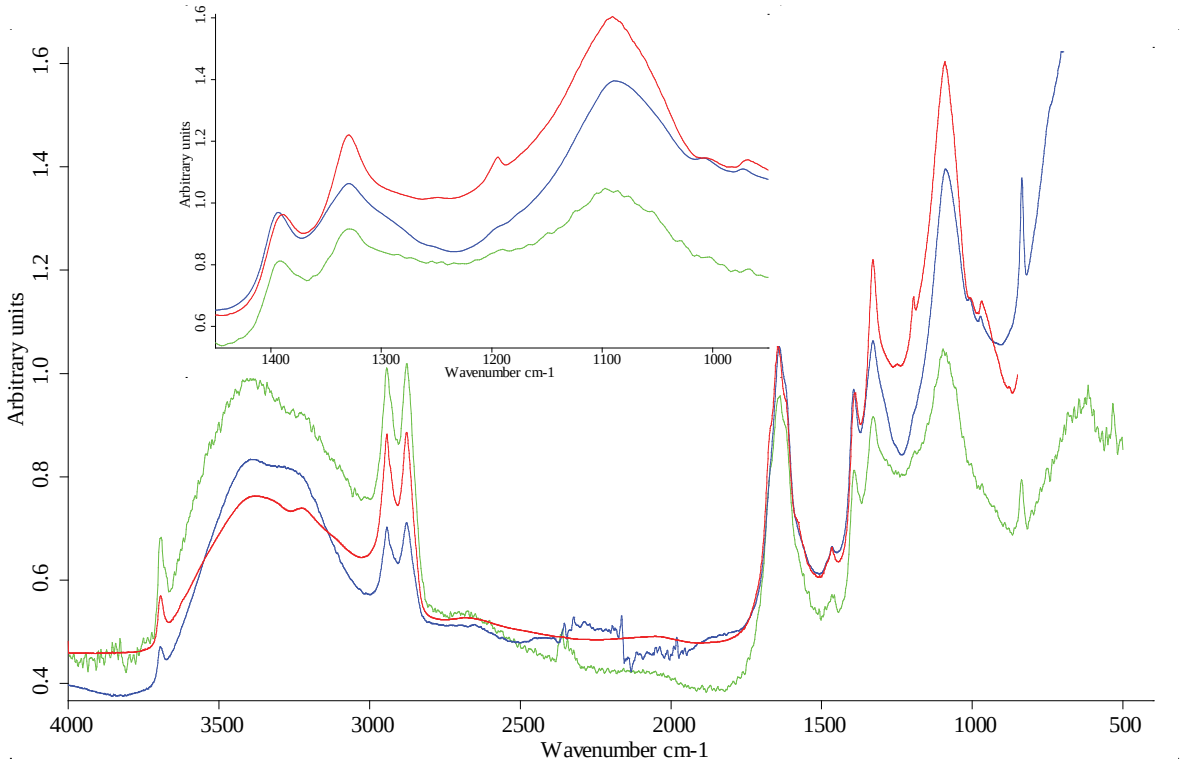

Figure 16. UDA-GO-SP-M1 nanodiamonds, red –ATR mode with photovoltaic MCT detector, blue – diffuse reflectance mode with photovoltaic MCT detector, green – photoacoustic mode. Spectra were not smoothed but normalized to maximize each spectrum.

Preprints (www.preprints.org) | NOT PEER-REVIEWED | Posted: 30 November 2020 doi:10.20944/preprints202011.0740.v1

Compared to ATR-FTIR, PAS-FTIR in general provides more informative spectra and shows the maximum sensitivity or resolution or both for absorption bands that do not have not enough sensitivity in ATR-IR spectra: the whole continuum of C=O stretch of carboxyl groups (1760 cm^{-1}) and better resolution in a complex band 1500–800 cm^{-1} with C-H, C-C, and C-O. Still, the comparison of PAS and DRIFT shows not many differences from the latter with a room-temperature DLaTGs detector and lower sensitivity compared to DRIFT with a photovoltaic detector. Along with a higher noise, PAS, especially at a single interferometer modulation frequency, cannot be recommended as a primary IR technique for nanodiamonds. Its main feature is lower dependence on the particle size due to large signal-penetration depth resulting from high thermal-conductivity of nanodiamond. Thus, it can be used a support/check technique for either DRIFT or ATR. Another feature of PAS, depth profiling with an IMF change obviously does not affect the spectra in a positive way and can be rather used for investigating thermal properties of nanodiamonds. Also, the disadvantages of this modality is a high penetration depth (up to 1 mm), which requires rather large sample volumes lest to have the effect of sample support on the spectra.

Thus, three scenarios can be considered: (1) an overall survey of nanodiamonds using the major bands of CH_x, water, and carboxyl groups; it may be implemented with any single modality. ATR is preferable from the simplicity and rapidity and does not require a sensitive detector; DRIFT can be used in all the conditions; PAS at a low IMF with a careful check of artefacts from gaseous water can be used. (2) Brand comparison by major and secondary bands (main surface moieties) to show the changes upon some surface modification, centrifugation, etc. Such a scenario requires two IR modalities; DRIFT as primary modality to have the maximum sensitivity of all the bands. ATR can also be used but requires a sensitive detector. DRIFT/ATR DRIFT/PAS or ATR/PAS can be used; PAS as a primary technique is not recommended due to a high noise level. (3) The case of a complete analysis of the surface required for applications of nanodiamonds, especially in biomedicine. In such scenario, all the modalities should be used. DRIFT with a high-sensitive detector and in NIR region to cross-check the major C-H HOH bands and with a spectrum in the region 2700-1900 cm-1; ATR at 2000–300 cm^{-1}. The region 1500–900 cm^{-1} is measured with DRIFT, ATR, and PAS (probably at two IMFs) to reveal possible artefact peaks, optical/thermal saturation, and revealing the nature of complex peaks can be comprised by hydrocarbon and functional groups).

In this aspect, the region of 1500–900 cm^{-1} should be further taken into account as the selected unmodified ND brands did not allow the final reliable information on the bands at 1470, 1440, 1400, 1370, 1330, 1270, 1210, 1190, 1140, 1100, 1050, 950 cm^{-1}; this would require a more detailed study with samples with known functional groups and a cross-comparison with other nanoparticle materials different from nanodiamonds.

Although it is not a direct comparison of IR modalities for NDs, it is noteworthy that CH_x bands at 3000–2800 and 1300 cm^{-1} (shoulder) of stretching and bending CH_x vibrations, respectively, do not disappear or change significantly upon drying, oxidizing by rather harsh conditions of acidic treatments [5] so they can be used as a kind of internal standard for quantification and brand comparison.

From the viewpoint of quantification, which was not considered in this study, some conclusions can be given: in general, most obvious application is the estimation of water and carbonyl contents aby the area 1900–1200 cm^{-1}. In this case, all the techniques showed enough sensitivity for the estimation and discrimination of various samples. Both ATR and DRIFT seem most expedient due to a low noise level and sensitivity. In the case of hydrocarbon contents, DRIFT shows the maximum possibility, especially with a photovoltaic detector due to high sensitivity and a satisfactory noise level. The identification shows that DRIFT can potentially be used for the discrimination of CH3 and alkane/alkene/aromatic CHX groups. This would require a reference method like NMR, elucidation of absorption coefficients for the ND materials of these bands, and working out the data handling for the quantification (most probably, integrated peak intensities should be used like it was shown for soil particles[31]). Among other possible quantification techniques are correlation studies between several counterparts of the functional groups like carboxyls at 2700, 1800, and 1400 cm^{-1}), studies of possible contributions of core groups at 2400–2200 cm^{-1} and quantification of ‘non-standard’ groups

 doi:10.20944/preprints202011.0740.v1

at 1600–1300 cm–1. In all these studies DRIFT with a high-sensitive detector is most expedient. The range 1100–400 cm^{-1}, though it contains some important information on NDs, seems most troublesome from the viewpoint of quantification due to possible optical and thermal-saturation effect, possible contributions of several functional groups and rather high noise levels in spectra. This requires some further studies before discussing the real possibilities. From the viewpoint of this study, the use of PAS for ND surface quantification seems less expedient compared to ATR and specially to DRIFT.

5. Conclusions

Thus, from the viewpoint of qualitative analysis of nanodiamond surface by FTIR spectrometry as was evaluated for rapid and nondestructive analysis and comparison of nanodiamonds, the analysis of ND surface requires all three modalities, diffuse-reflectance, attenuated total reflection, and photoacoustic modalities: DRIFT provides the maximum number of bands among all three modalities and is capable of measuring hydrogen-bonded bands and CH_x groups. ATR provides the required sensitivity for water absorption band and C–O–H bands but is not sensitive in the range 4000–2000 cm^{-1}. PAS-FTIR reveals fewer bands than DRIFT but more bands than ATR-FTIR and provides the information less dependent on the particle size.

Author Contributions: For research articles with several authors, a short paragraph specifying their individual contributions must be provided. The following statements should be used "Conceptualization, D.V. methodology, D.V.; formal analysis, M.P. and D.V.; investigation, D.V. and P.K.; resources, D.V..; data curation, D.V.; writing—original draft preparation, M.P., D.V. and P.K.; writing—review and editing, M.P. and D.V.; visualization, D.V and P.K..; supervision, M.P.; project administration, D.V.; funding acquisition, D.V. All authors have read and agreed to the published version of the manuscript.

Funding: This work was funded by the Russian Foundation for Basic Research (RFBR) and Moscow City Government according to the research project no. 19-33-70068 mol_a_mos.

Conflicts of Interest: The authors declare no conflict of interest.

Appendix A

Preprints (www.preprints.org) | NOT PEER-REVIEWED | Posted: 30 November 2020 doi:10.20944/preprints202011.0740.v1

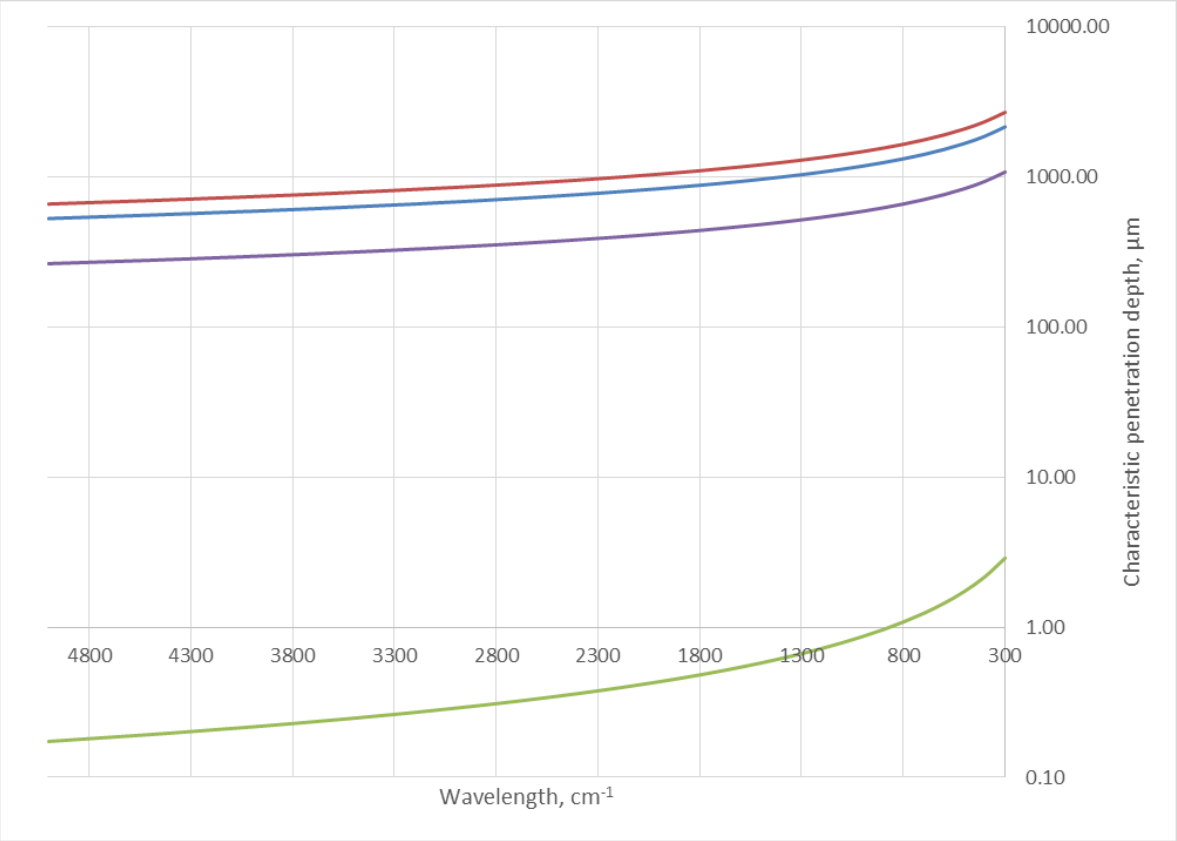

Figure S1. Radiation penetration depth into nanodiamond sample for ATR (green curve) and photoacoustic IR measurements at interferometer modulation frequencies 1.6 (red), 2.5 (blue) and 10 kHz (violet line).

References

1. Buchatskaya, Y., et al., *Sorption of actinides onto nanodiamonds.* Radiochimica Acta, 2015. **103**(3).
2. Stehlik, S., et al., *Size and Purity Control of HPHT Nanodiamonds down to 1 nm.* J Phys Chem C Nanomater Interfaces, 2015. **119**(49): p. 27708-27720.
3. Peristyy, A., et al., *Ion-exchange properties of High Pressure High Temperature synthetic diamond.* Diamond and Related Materials, 2017. **75**: p. 131-139.
4. Peristyy, A., B. Paull, and P.N. Nesterenko, *Ion-exchange properties of microdispersed sintered detonation nanodiamond.* Adsorption, 2016. **22**(3): p. 371-383.
5. Volkov, D.S., et al., *Pristine detonation nanodiamonds as regenerable adsorbents for metal cations.* Diamond and Related Materials, 2020. **110**: p. 108121.
6. Dolmatov, V.Y., *Detonation-synthesis nanodiamonds: synthesis, structure, properties and applications.* Russian Chemical Reviews, 2007. **76**(4): p. 339-360.
7. Chernysheva, M.G., et al., *Cationic surfactant coating nanodiamonds: Adsorption and peculiarities.* Colloids and Surfaces A: Physicochemical and Engineering Aspects, 2019. **565**: p. 25-29.
8. Shenderova, O.A. and D.M. Gruen, *Ultrananocrystalline Diamond*. 2nd ed. Synthesis, Properties and Applications. 2012: Elsevier Inc.
9. Zhang, K., et al., *Nanodiamonds conjugated upconversion nanoparticles for bio-imaging and drug delivery.* J Colloid Interface Sci, 2019. **537**: p. 316-324.
10. Qin, S.-R., et al., *Rare earth-functionalized nanodiamonds for dual-modal imaging and drug delivery.* Diamond and Related Materials, 2019. **91**: p. 173-182.

11. Mochalin, V.N., et al., *Adsorption of drugs on nanodiamond: toward development of a drug delivery platform.* Mol Pharm, 2013. **10**(10): p. 3728-35.
12. Ţucureanu, V., A. Matei, and A.M. Avram, *FTIR Spectroscopy for Carbon Family Study.* Critical Reviews in Analytical Chemistry, 2016. **46**(6): p. 502-520.
13. Sun, X., et al., *New insights into the oxidative dehydrogenation of propane on borate-modified nanodiamond.* Chem Commun (Camb), 2015. **51**(44): p. 9145-8.
14. Remes, Z., et al., *Diamond-coated ATR prism for infrared absorption spectroscopy of surface-modified diamond nanoparticles.* Applied Surface Science, 2013. **270**: p. 411-417.
15. Stehlik, S., et al., *Water interaction with hydrogenated and oxidized detonation nanodiamonds — Microscopic and spectroscopic analyses.* Diamond and Related Materials, 2016. **63**: p. 97-102.
16. Petit, T. and L. Puskar, *FTIR spectroscopy of nanodiamonds: Methods and interpretation.* Diamond and Related Materials, 2018. **89**: p. 52-66.
17. Mayerhofer, T.G., H. Mutschke, and J. Popp, *Employing Theories Far beyond Their Limits-The Case of the (Boguer-) Beer-Lambert Law.* Chemphyschem, 2016. **17**(13): p. 1948-55.
18. Zhang, J., et al., *Surface chemistry and catalytic reactivity of a nanodiamond in the steam-free dehydrogenation of ethylbenzene.* Angew Chem Int Ed Engl, 2010. **49**(46): p. 8640-4.
19. A. Beyler-Çiğil, E.Ç., M. Vezir Kahraman, *Thermal properties of phosphorylated nanodiamond reinforced polyimides.* Polymer Composites, 2016. **37**(8): p. 2285-2292.
20. H. A. Girard, S.P., C. Gesset, M. Chaigneau, L. Vieille, J. C. Arnault, P. Bergonzo, J. P. Boilot, T. Gacoin, *Electrostatic grafting of diamond nanoparticles: a versatile route to nanocrystalline diamond thin films.* ACS Appl Mater Interfaces, 2009. **1**(12): p. 2738-46.
21. Frosch, T., et al., *Nondestructive three-dimensional analysis of layered polymer structures with chemical imaging.* Langmuir, 2010. **26**(24): p. 19027-32.
22. A. G. Inel, E.M.U., *Solvent–surface interactions between nanodiamond and ethanol studied with in situ infrared spectroscopy.* Diamond and Related Materials, 2016. **61**: p. 7-13.
23. Xing, Z., et al., *Agricultural soil characterization by FTIR spectroscopy at micrometer scales: Depth profiling by photoacoustic spectroscopy.* Geoderma, 2019. **335**: p. 94-103.
24. Bauer, A., et al., *IR-spectroscopy of skin in vivo: Optimal skin sites and properties for non-invasive glucose measurement by photoacoustic and photothermal spectroscopy.* Journal of Biophotonics, 2018. **11**(1).
25. Brangule, A., et al., *In Vitro Characterization Perspectives Using Fourier Transform Infrared Photoacoustic Spectroscopy (FTIR-PAS) and Diffuse Reflectance Infrared Spectroscopy (DRIFT).* Key Engineering Materials, 2017. **758**: p. 273-277.
26. Kizil, R. and J. Irudayaraj, *Fourier Transform Infrared Photoacoustic Spectroscopy (FTIR-PAS)*, in *Encyclopedia of Biophysics*, G.C.K. Roberts, Editor. 2013, Springer Berlin Heidelberg: Berlin, Heidelberg. p. 840-844.
27. Michaelian, K.H. and Q. Wen, *Photoacoustic infrared spectroscopy of solids.* Journal of Physics: Conference Series, 2010. **214**.
28. Ando Toshihiro, I.S., Ishii Motohiko, *Fourier-transform infrared photoacoustic studies of hydrogenated diamond surfaces.* Journal of the Chemical Society, Faraday Transactions, 1993. **89**(4).
29. Ando, T., et al., *Fourier-transform infrared photoacoustic studies of hydrogenated diamond surfaces.* Journal of the Chemical Society, Faraday Transactions, 1993. **89**(4).

30. Pasieczna-Patkowska, S. and J. Madej, *Comparison of photoacoustic, diffuse reflectance, attenuated total reflectance and transmission infrared spectroscopy for the study of biochars.* Polish Journal of Chemical Technology, 2018. **20**(4): p. 75-83.
31. Krivoshein, P.K., et al., *FTIR photoacoustic spectroscopy for identification and assessment of soil components: Chernozems and their size fractions.* Photoacoustics, 2020. **18**: p. 100162.
32. Du, C. and J. Zhou, *Application of infrared photoacoustic spectroscopy in soil analysis.* Applied Spectroscopy Reviews, 2011. **46**(5): p. 405-422.
33. Michaelian, K.H., *Photoacoustic IR Spectroscopy: Instrumentation, Applications and Data Analysis*. 2nd, Revised and Enlarged Edition ed. 2010, Weinheim, Germany: Wiley-VCH. 402.
34. Tokmakoff, A., W.F. Banholzer, and M.D. Fayer, *Thermal diffusivity measurements of natural and isotopically enriched diamond by picosecond infrared transient grating experiments.* Applied Physics A Solids and Surfaces, 1993. **56**(1): p. 87-90.
35. Heaney, P.J., et al., *Chapter 4. HYDROGEN SPECIATION AND CHEMICAL WEAKENING OF QUARTZ*, in *Silica*. 1994, De Gruyter. p. 123-176.
36. Spitsyn, B.V., et al., *Inroad to modification of detonation nanodiamond.* Diamond and Related Materials, 2006. **15**(2-3): p. 296-299.
37. Calderón, F.J., et al., *Diffuse-Reflectance Mid-infrared Spectral Properties of Soils under Alternative Crop Rotations in a Semi-arid Climate.* Communications in Soil Science and Plant Analysis, 2011. **42**(17): p. 2143-2159.
38. Hadži, D. and M. Pintar, *The OH in-plane deformation and the C-O stretching frequencies in monomeric carboxylic acids and their association shifts.* Spectrochimica Acta, 1958. **12**(2): p. 162-168.
39. Asselin, M. and C. Sandorfy, *Anharmonicity and Hydrogen Bonding. The in-plane OH Bending and its Combination with the OH Stretching Vibration.* Canadian Journal of Chemistry, 1971. **49**(9): p. 1539-1544.
40. Hens, S.C., et al., *Nanodiamond bioconjugate probes and their collection by electrophoresis.* Diamond and Related Materials, 2008. **17**(11): p. 1858-1866.
41. Colthup, N.B., L.H. Daly, and S.E. Wiberley, *Introduction to Infrared and Raman Spectroscopy*. 1990: Elsevier Science.
42. Mitev, D., et al., *Surface peculiarities of detonation nanodiamonds in dependence of fabrication and purification methods.* Diamond and Related Materials, 2007. **16**(4-7): p. 776-780.
43. T. Jiang, K.X., *FTIR study of ultradispersed diamond powder synthesized by explosive detonation* Carbon, 1995. **33**(12): p. 1663-1671.
44. Korobov, M.V., et al., *Improving the dispersity of detonation nanodiamond: differential scanning calorimetry as a new method of controlling the aggregation state of nanodiamond powders.* Nanoscale, 2013. **5**(4): p. 1529-1536.
45. Tu, J.S., et al., *Size-dependent surface CO stretching frequency investigations on nanodiamond particles.* J Chem Phys, 2006. **125**(17): p. 174713.
46. Volkov, D.S., M.A. Proskurnin, and M.V. Korobov, *Elemental analysis of nanodiamonds by inductively-coupled plasma atomic emission spectroscopy.* Carbon, 2014. **74**: p. 1-13.
47. Volkov, D.S., M.A. Proskurnin, and M.V. Korobov, *Survey study of mercury determination in detonation nanodiamonds by pyrolysis flameless atomic absorption spectroscopy.* Diamond and Related Materials, 2014. **50**: p. 60-65.
48. Max, J.J. and C. Chapados, *Isotope effects in liquid water by infrared spectroscopy. III. H2O and D2O spectra from 6000 to 0 cm(-1).* J Chem Phys, 2009. **131**(18): p. 184505.

49. Gibson, N., et al., *Colloidal stability of modified nanodiamond particles.* Diamond and Related Materials, 2009. **18**(4): p. 620-626.
50. Chung, K. and S. Tomljenovic-Hanic, *Emission Properties of Fluorescent Nanoparticles Determined by Their Optical Environment.* Nanomaterials, 2015. **5**(2): p. 895-905.
51. Batsanov, S.S., et al., *Structural changes in colloid solutions of nanodiamond.* New Journal of Chemistry, 2020. **44**(4): p. 1640-1647.
52. Usoltseva, L.O., et al., *Absorption spectra of nanodiamond aqueous dispersions by optical absorption and optoacoustic spectroscopies.* Photoacoustics, 2018. **12**: p. 55-66.
53. Charles Q. Yang, W.G.F., *The effect of particle size on Fourier-transform infrared photoacoustic spectra.* Journal of Molecular Structure, 1986. **146**: p. 25-39.
54. T. Jiang, K.X., *FTIR study of ultradispersed diamond powder synthesied by explosive detonation.* Carbon, 1995. **33**(12): p. 1663-1661.
55. Podobedov, V., et al., *Calibration of spectral responsivity of IR detectors in the range from 0.6 μm to 24 μm*. SPIE Defense + Security. Vol. 9819. 2016: SPIE.
56. Nguyen, T.T., L.J. Janik, and M. Raupach, *Diffuse reflectance infrared fourier transform (DRIFT) spectroscopy in soil studies.* Soil Research, 1991. **29**(1): p. 49-67.
57. Deb, P., et al., *Correlating Nitrile IR Frequencies to Local Electrostatics Quantifies Noncovalent Interactions of Peptides and Proteins.* The Journal of Physical Chemistry B, 2016. **120**(17): p. 4034-4046.
58. Begue, D., G.G. Qiao, and C. Wentrup, *Nitrile imines: matrix isolation, IR spectra, structures, and rearrangement to carbodiimides.* J Am Chem Soc, 2012. **134**(11): p. 5339-50.
59. Fang, C., et al., *Preparation of "natural" diamonds by HPHT annealing of synthetic diamonds.* CrystEngComm, 2018. **20**(4): p. 505-511.
60. McClelland, J.F., et al., *Photoacoustic Spectroscopy*, in *Handbook of Vibrational Spectroscopy*, J.M. Chalmers and P.R. Griffiths, Editors. 2006, Wiley.
61. Calderón, F.J., et al., *Chemical Differences in Soil Organic Matter Fractions Determined by Diffuse-Reflectance Mid-Infrared Spectroscopy.* Soil Science Society of America Journal, 2011. **75**(2): p. 568-579.
62. Morterra, C. and M.J.D. Low, *The Nature of the 1600 cm−1Band of Carbons.* Spectroscopy Letters, 2006. **15**(9): p. 689-697.
63. Seredych, M., J.A. Rossin, and T.J. Bandosz, *Changes in graphite oxide texture and chemistry upon oxidation and reduction and their effect on adsorption of ammonia.* Carbon, 2011. **49**(13): p. 4392-4402.
64. Navarro-Pardo, F., et al., *Effects on the Thermo-Mechanical and Crystallinity Properties of Nylon 6,6 Electrospun Fibres Reinforced with One Dimensional (1D) and Two Dimensional (2D) Carbon.* Materials (Basel), 2013. **6**(8): p. 3494-3513.
65. Bertaux, J., F. Froehlich, and P. Ildefonse, *Multicomponent analysis of FTIR spectra; quantification of amorphous and crystallized mineral phases in synthetic and natural sediments.* Journal of Sedimentary Research, 1998. **68**(3): p. 440-447.
66. Brown, D.J., et al., *Global soil characterization with VNIR diffuse reflectance spectroscopy.* Geoderma, 2006. **132**(3): p. 273-290.